Source parameters of laboratory acoustic emission events estimated from the coda of waveforms

Tatiana I. Kartseva[1,2], Nikolai M. Shapiro[1], Andrey V. Patonin[3], Natalia M. Shikhova[3], Vladimir B. Smirnov[2,4], Alexander V. Ponomarev[2]

[1]Institut des Sciences de la Terre, Univ. Grenoble Alpes, CNRS, Univ. Savoie Mont Blanc, IRD, Univ. Gustave Eiffel, 38400, Grenoble, France
[2]Schmidt Institute of Physics of the Earth, Russian Academy of Sciences, 123995, Moscow, Russia
[3]CPGR Geophysical observatory "Borok", 152742, Borok, Russia
[4]Lomonosov Moscow State University, 119234, Moscow, Russia

Key Points:

- Coda of acoustic emission (AE) waveforms can be used for the source characterization.
- Scaling between the corner frequency f_c and seismic moment M_0 varies in function of loading regime and rock type.
- The $M_0 - f_c$ scaling of AE events was found similar to that of tectonic earthquakes when isotropic confining pressure applied to intact rocks.

Corresponding author: Tatiana I. Kartseva, `tatiana.kartseva@univ-grenoble-alpes.fr`

Abstract

We develop a method to estimate relative seismic moments M_0 and corner frequencies f_c of acoustic emission events recorded in laboratory experiments from amplitude spectra of signal's coda composed of reverberated and scattered waves. This approach has several advantages with respect to estimations from direct waves that are often clipped and also are difficult to separate in experiments performed on small samples. Also, inversion of the coda spectra does not require information about the source locations ans mechanisms. We use the developed method to analyze the data of two experiments: (1) on granite from the Voronezh crystal massif and (2) on Berea sandstone. The range of absolute corner frequencies estimated in both experiments is around 70–700 kHz. The range of relative seismic moments covers $10^{3.5}$. The relation between f_c and M_0 observed on the first stages of both experiments, consisted of increasing isotropic confining pressure, approximately follow $M_0 \sim f_c^{-3}$ scaling and the *b-value* of the Gutenberg-Richter distribution was found close to 1. This can be interpreted as rupturing of preexisting material defects with a nearly constant stress-drop and has a similarity with observations of "natural" earthquakes. Deviations from this "earthquake-like" behavior observed after applying axial loading and initiation of sample damaging can be interpreted as changes in stress-drop. Lower stress-drops prevail for sandstone and higher for granite sample respectively that can be related to the strength of corresponding material.

Plain Language Summary

Earthquakes generation mechanisms and conditions favoring their occurrence are still debated. Inability to observe these processes in-situ and long lasting earthquake preparation period favor using laboratory experiments to verify quickly the adequacy of proposed hypotheses. Fracturing of small rock samples with high pressures and recording acoustic waves from their micro-fractures is among them. In most cases, the laboratory acoustic emission (AE) is analyzed and compared to natural seismicity statistically, demonstrating similar Gutenberg-Richter power-law magnitude distribution. More advanced analyses can include source characteristics (corner frequencies, seismic moments, and stress-drops), responsible for the source size, forces acting there and stress changes. Ensembles of these characteristics can give ideas on the common generation mechanisms. In laboratory, several technical limitations slow down the implementation of such analyses, widely used in Earth's seismology. We propose a method that use coda waves (signal's decaying part) to estimate source parameters of the laboratory AE. We tested it on two similar experiments conducted on different rock types. Source analyses revealed the high similarity of well-studied tectonic earthquakes and fracturing of pre-existing inhomogeneties in the rock samples by applying equally distributed external pressure to it. The active production of new fractures under high one-directional pressure in contrary deviated significantly.

1 Introduction

Since early studies in 1960s (e.g., Scholz, 1968), impulsive acoustic emission events observed during the rock physics experiments are often considered as analog of natural earthquakes and are used to study the seismogenic processes in controlled laboratory conditions (e.g., Lockner et al., 1991; McLaskey & Kilgore, 2013; Yoshimitsu et al., 2014; V. B. Smirnov et al., 2019; Bolton et al., 2023; Marty et al., 2023). Analyses of large catalogs of "laboratory earthquakes" demonstrated that they obey statistical distributions similar to "natural" earthquakes. The size-frequency distribution of acoustic emission events follows the power-law Gutenberg Richter relationship (Gutenberg & Richter, 1944) and exhibit aftershock sequences governed by the Omori law (Omori, 1894). The former is often considered as manifestation of self-similarity of earthquakes occurring at different scales. One of the main parameters measured in the experiments aimed at under-

standing the laboratory seismicity is the Gutenberg-Richter's "b-value" whose variations are interpreted in a relationship with loading conditions and material properties leading to attempts of analogies with natural earthquakes occurrence and their eventual prediction.

While built from very large amounts of events, the most of acoustic emission catalogs contain limited numbers of their parameters. In addition to event times, their magnitudes and hypocenter locations (when recorded by a sufficient number of receivers) are most frequently reported. However, the magnitudes are in most of cases determined from records by poorly calibrated sensors and cannot be simply related to physical source parameters. So far, advanced analyses requiring well characterized source spectra, focal mechanisms, etc are rarely performed on acoustic emission data.

In earthquake seismology, advanced analyses of seismograms and their spectra are used to measure various physical source parameter such as magnitudes, seismic rupture dimensions, seismic energy (e.g., Båth, 1966) and scalar seismic moment (e.g., Aki, 1966). Systematic determination of these different parameters for "regular" tectonic earthquakes resulted in establishing simple scaling relationships between them (e.g., Aki, 1967; Kanamori & Anderson, 1975; Abercrombie, 1995). These "earthquakes scaling laws" remain valid over several orders of magnitudes and lead to a concept of self-similarity of seismic ruptures under constant average stress drop. Together with a simple geometrical argument this gives the Gutenberg Richter distribution with $b = 1$. In this paper, we will refer to a simultaneous observation of the earthquakes scaling laws pointing to constant stress-drop and of *b-value* close to 1 as a "regular earthquake regime".

The average stress drops inferred for tectonic earthquakes approximately lie in the range of 1 to 10 MPa (equivalent strain drops being between 10^{-5} and 10^{-4}) (e.g., Kanamori & Anderson, 1975; Allmann & Shearer, 2009), which is significantly smaller than the strength of the crustal rocks and the values geologically observed in the field for the faults (Schlische et al., 1996). All this is in good agreement with the conceptual model when tectonic earthquakes are not produced by fresh ruptures but occur on pre-existing and on average "weak" faults.

At the same time, there are various types of seismicity with properties different from the "regular earthquake regime" mentioned above. One example are the volcanic earthquakes that often do not follow the Gutenberg Richter distribution with $b = 1$ (e.g., Galina et al., 2020; Jacobs & McNutt, 2010; Wyss et al., 1998) Another example is provided by the induced seismicity with reported stress drops being very variable (e.g., Lengliné et al., 2014; Wu et al., 2018; Shapiro & Dinske, 2021). Finally, the scaling laws for recently discovered slow earthquakes are often reported being different from those known for "regular" earthquakes (e.g., Ide et al., 2007; Peng & Gomberg, 2010; Bostock et al., 2015; Farge et al., 2020; Ide & Beroza, 2023). Also, some studies have found deviations from "regular" scaling laws for tectonic earthquakes (Mayeda et al., 2007). Such behavior might be considered as manifestations of different seismogenic mechanisms and mechanical behaviors of involved rocks.

An accurate interpretation of analyses of the laboratory acoustic emission and its comparison with different types of natural seismicity would benefit from more systematically determined physical source parameters similar to approaches used in the earthquake seismology. To achieve this, the spectral analysis of acoustic emission signals is sometimes performed to measure the event seismic moments and corner frequencies (inversely proportional to source time duration and its linear size). However, such an analyses is not routine. The reason is various limitations of laboratory experiment, including resonance of acoustic piezo-transducers, complicated absolute calibration, limited frequency range, limited sample sizes and, accordingly, the configuration of the transducer recording system.

The absolute estimations of corner frequencies and seismic moments was obtained by McLaskey and Lockner (2016) with calibrating sensors on the impact spectrum of a falling steel ball. The laser calibration of sensors was carried out by Yoshimitsu et al. (2014) and Marty et al. (2023) to obtain source characteristics of bigger set of AE-events. In (Yoshimitsu et al., 2014) the cubic relation between seismic moment and source duration has been verified but in the same time the b-value of Gutenberg-Richter has been estimated as 2. Results of Marty et al. (2023) have shown the stress-drops tending to increase for larger events. The similar problem has been revealed in Blanke et al. (2020). Harrington and Benson (2011) obtained cubic moment-duration relation for dry experiment and strong deviation from it in wet samples. Overall, the verification of "earthquake" scaling lows for these small laboratory-scale sources remains an open question.

With the available laboratory experiment performed on relatively small samples, the use of direct waves as it has been done in all works mentioned above is impossible due to the limitations that will be described in detail in the section "Limitations of laboratory AE-signal". Therefore, in this work the use of the signal's coda is proposed as alternative to direct waves. In earthquakes seismology, such coda-based approach was successfully applied for estimation of earthquake source spectra (e.g., Rautian & Khalturin, 1978; Mayeda & Walter, 1996). Although the acoustic coda in laboratory experiments has a slightly different formation mechanism (e.g., Farin et al., 2016; T. I. Kartseva et al., 2022) it still can be used to estimate the source spectra and their main parameters. To validate the method, we apply it to the data of two experiments: (1) on granite from the Voronezh crystal massif and (2) on Berea sandstone.

2 Earthquake Scaling Laws and Spectral Analysis

The seismic moment M_0 is defined as:

$$M_0 = \mu S D \tag{1}$$

where μ is the shear modulus, S is the rupture surface, and D is the slip amplitude (Aki, 1966). Therefore, M_0 is related to the source size giving rise to a physical magnitude scale (Hanks & Kanamori, 1979):

$$M_W = 2/3 \lg M_0 + const \tag{2}$$

One of the main scaling laws is the relationship between seismic moment and the linear rupture dimension L (or rupture surface) (Kanamori & Anderson, 1975):

$$M_0 \sim L^3 \sim S^{3/2} \tag{3}$$

Combination of (1) and (3) implies the constant average stress drop during earthquakes:

$$\Delta\sigma = C\mu D/L = const \tag{4}$$

where C is a non-dimensional geometrical shape factor and D/L being a strain drop. By combining equations (2) and (3) we obtain that under constant strain (stress) drop the magnitude is linearly proportional to the logarithm of the rupture surface with a proportionality coefficient equal to 1.

Following (Kanamori & Anderson, 1975), more small ruptures can be accommodated on a total fault area Σ. In other words the product of number of earthquakes N_S with source area S and of this area should be approximately equal to the total fault area:

$N_S S \sim \Sigma$, implying that N_s is inversely proportional to the source area. When combined with the linear proportionality between the magnitude and the logarithm of the source area under constant stress drop, this gives the Gutenberg Richter distribution with $b = 1$:

$$\lg N = -bM_w + a \ , \quad b = 1 \tag{5}$$

For most of earthquakes, the rupture linear dimensions cannot be directly measured. Instead, the source duration in time t_c, that is approximately equal to L/V_r (V_r being the rupture propagation velocity) can be inferred from analysing seismograms or their spectra. The latter can be corrected for the propagation effects and the radiation pattern to retrieve the frequency dependent source term. The form of this term can be predicted from simple source models (e.g. Haskell, 1964; Brune, 1970; Boatwright, 1980) and is characterized by two asymptotics. At low frequencies, the displacement spectra converges to a plateau whose level is proportional to the seismic moment. At high frequencies, the spectral amplitude is characterized by a power-low decay. The transition between this two asymptortics occurs at the vicinity of so called cut-off or corner frequency f_c that is inversely proportional to the source time duration. As a consequence, the invariance of the seismic rupture stress drop can be expressed via a scaling relationship between the seismic moment and the corner frequency (e.g. Aki, 1967):

$$M_0 \sim f_c^{-3} \tag{6}$$

Analysis of spectra has been applied to many real seismic datasets and the cubic moment - corner frequency relation has been observed for large and moderate (e.g. Allmann & Shearer, 2009; Ross & Ben-Zion, 2016) to small (with $M_W < 3$) (e.g. Abercrombie, 1995; Prieto et al., 2004) earthquakes, and for the mine seismicity (events of magnitudes $-4 < M_W < 0$) (e.g. Kwiatek et al., 2011). The spectral method of determination of source parameters has been also applied to slow earthquakes (e.g. Bostock et al., 2015; Farge et al., 2020; Supino et al., 2020).

3 Data

3.1 Set-up and Experiments

We use the acoustic data recorded during pseudo-triaxial tests of cylindrical rock samples, carried out on the controlled hydraulic press INOVA-1000 GO "Borok" IPE RAS (A. Patonin et al., 2014; A. V. Patonin et al., 2019). The cylindrical sample of $60mm$ height and $30mm$ diameter is sealed against penetration of confining oil to the pore space and installed in a cell with 16 ultrasonic sensors. The diameter of sensor body is around $5mm$, the contact surface is curved in accordance to the sample surface and tightly pressed to it. The cell is installed inside the confining pressure chamber and placed between the punches of press (Fig. 1).

We consider two experiments that were carried out on Berea sandstone (porosity 17%) and Voronezh granite samples (porosity 0.6%) with similar loading conditions that can be divided into 4 similar stages (Fig. 2). First stages of both experiments are the same: applying 4 confining pressure P_c steps ($+2MPa, +2MPa, +4MPa, +4MPa$) to the intact rock samples. During the stages II the differential stress σ is applied under constant P_c and controlled by the acoustic emission activity to provide quasi-static fault growing. While in Sandstone experiment after reaching around 90% of sample's strength the macro-fault was formed instantly, the Granite sample was able to sustain a cycle of slips along fault. During stages III another 4 steps $2MPa$ each were applied to the damaged rock samples. This stage has strengthen samples (note the increase in P-wave velocities) before final axial loading IV.

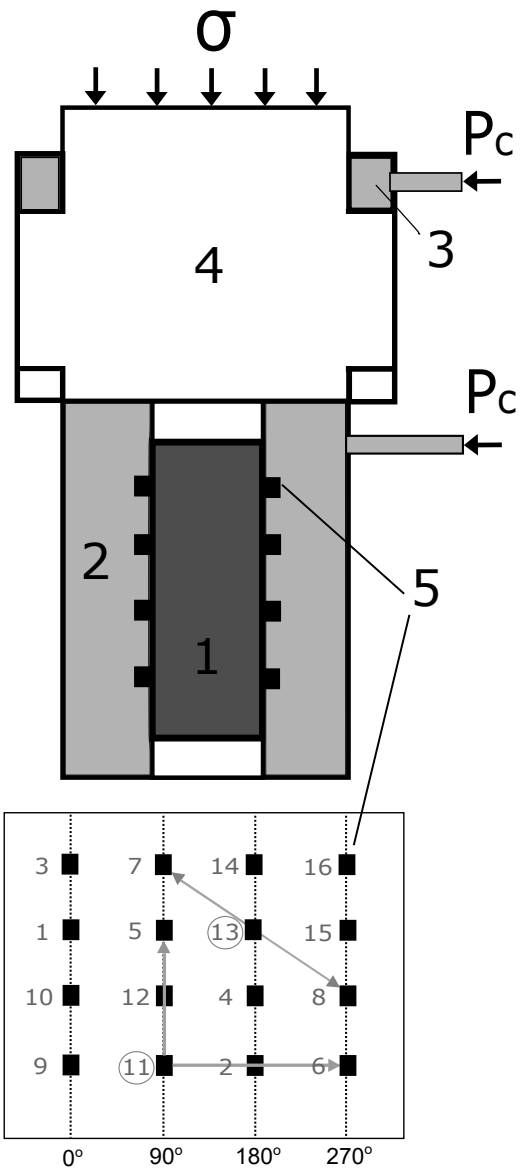

Figure 1. Schematic representation of the experimental set-up. 1 – rock sample; 2 – confining pressure chamber; 3 – compensator providing external pressure equal to Pc at the top of the sample; 4 – press providing axial load σ; 5 – system of 16 piezo-sensors (layout is shown at the bottom). At the bottom: numbers of sensors in gray, examples of ultrasonic sounding traces of two emmiters 11 and 13 sending elastic impulse to corresponding receivers 5 and 6, 7 and 8

Acoustic emission is recorded by a system of side sensors with low-noise pre-amplifying and analog-to-digital converter (ADC) programmed for the pre-triggering mode (sampling rate $2.5\,MHz$). The acoustic signal is continuously digitized into the ring buffer of ADC. Right after the first signal arrival exceeding the amplitude threshold from any of 16 channels the data block containing $255\,\mu s$ before the first arrival and $360\,\mu s$ after is sent to the storage. Therefore for each event with the signal amplitude enough to trigger the system there are 16 waveforms of $615\,\mu s$ duration with the start time shifted to $255\,\mu s$ of the standard record frame (Fig. 3a, b). Noise and signal Fourier amplitude spectra (Fig. 3e and f) for corresponding records from the first three sensors demonstrate the frequency range limitation: up to around $30\,kHz$ by the noise of the hydraulic press and above around $600kHz$ by strong absorption of waves starting from about $600\,kHz$.

Besides recording of acoustic emission the system is periodically (around each $22\,sec$) switched to the ultrasonic sounding mode. In this mode during the period of $1.5-22\,sec$ 8 sensors serve as emitters of artificial elastic impulse while other 8 ones receive these signals crossing the sample in different directions (Fig. 1). Having a total 16 paths and measured travel times every $22\,sec$ allows to calculate time-dependent distribution of elastic wave velocities, that is necessary for the event location procedure. Time evolution of average P-wave velocities is shown with black lines in Fig. 2. Location of AE-events is based on determination of arrival times of AE-signals (by STA/LTA or AIC-picker methods, depending on which one worked better) and minimizing travel times while searching the location in the space grid in the sample (for details A. Patonin et al. (2014)).

During the 4 stages of granite and sandstone experiments 36162 and 53698 acoustic emission waveforms were recorded, respectively.

3.2 Limitations of Laboratory AE-Signals

The experimental setup that we use has several limitations in terms of the quality of the acoustic emission waveforms. The first one and most obvious is clipping of the signals of strongest AE-events due to the limited dynamic range of the ADC (Fig. 3b). The second limitation consists in the inability to separate clearly direct waves from the coda (waves reflected from the sample surfaces. Main reason for this is the small size of the sample that comparable with the used wavelengths. Resulting arrival times of the reflected waves around $10-15\mu s$ ($60\,mm/(3.5-4)km/s$) which is very close to the duration of the direct waves signal (Fig. 3a and b).

4 Estimation of Source Parameters from the Coda of AE-Signals

Signal recorded during event i at sensor j can be represented as:

$$y_i^j(t) = s_i(t_i, t) * g_{i,j}(t - t_i) * r_j(t - t_i) \tag{7}$$

where $s_i(t_i, t)$ is the source time function of an acoustic emission event i that occurs at time t_i, $g_{i,j}(t-t_i)$ is the Green's function characterizing the wave propagation between the source i and sensor j, and $r_j(t - t_i)$ is the response of the receiver j. In the spectral domain this equation becomes:

$$Y_i^j(f) = S_i(f)\, G_{i,j}(f)\, R_j(f) \tag{8}$$

where f is the frequency and $S_i(f)$ is the source spectra that we would like to retrieve. Thus, a deconvolution of the sensor response and of the propagation term must be applied to the recorded signals (or their spectra). In the earthquake seismology, the source parameters are most often retrieved from direct waves. This requires knowing the source

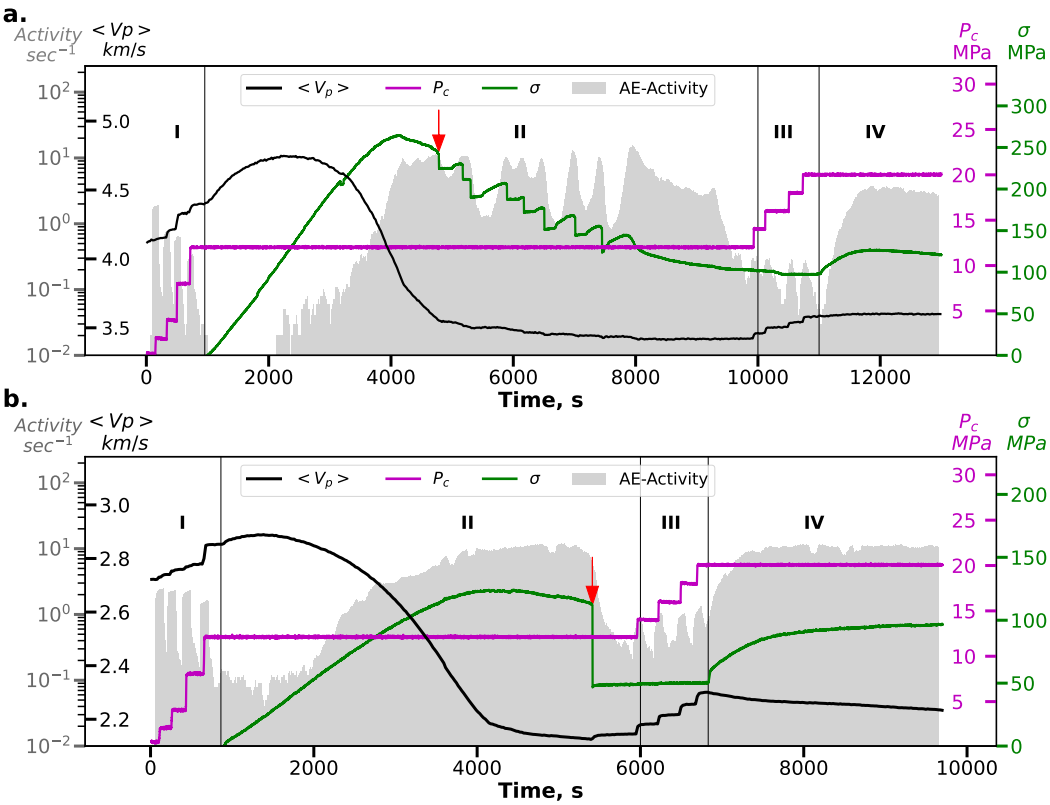

Figure 2. Loading history of Garnite (a) and Sandstone (b) experiments divided by 4 stages I-IV. *Left axis:* black curves $< V_p >$ - P-wave velocities averaged over 16 traces, gray bars showing activity of acoustic emission calculated as 100 events divided by the time period they occur. Red arrows point the onset of macro-faulting (4781s for Granite and 5411s for Sandstone). *Right axis:* magenta curves P_c - confining pressure, green curves σ - differential stress (Fig. 1).

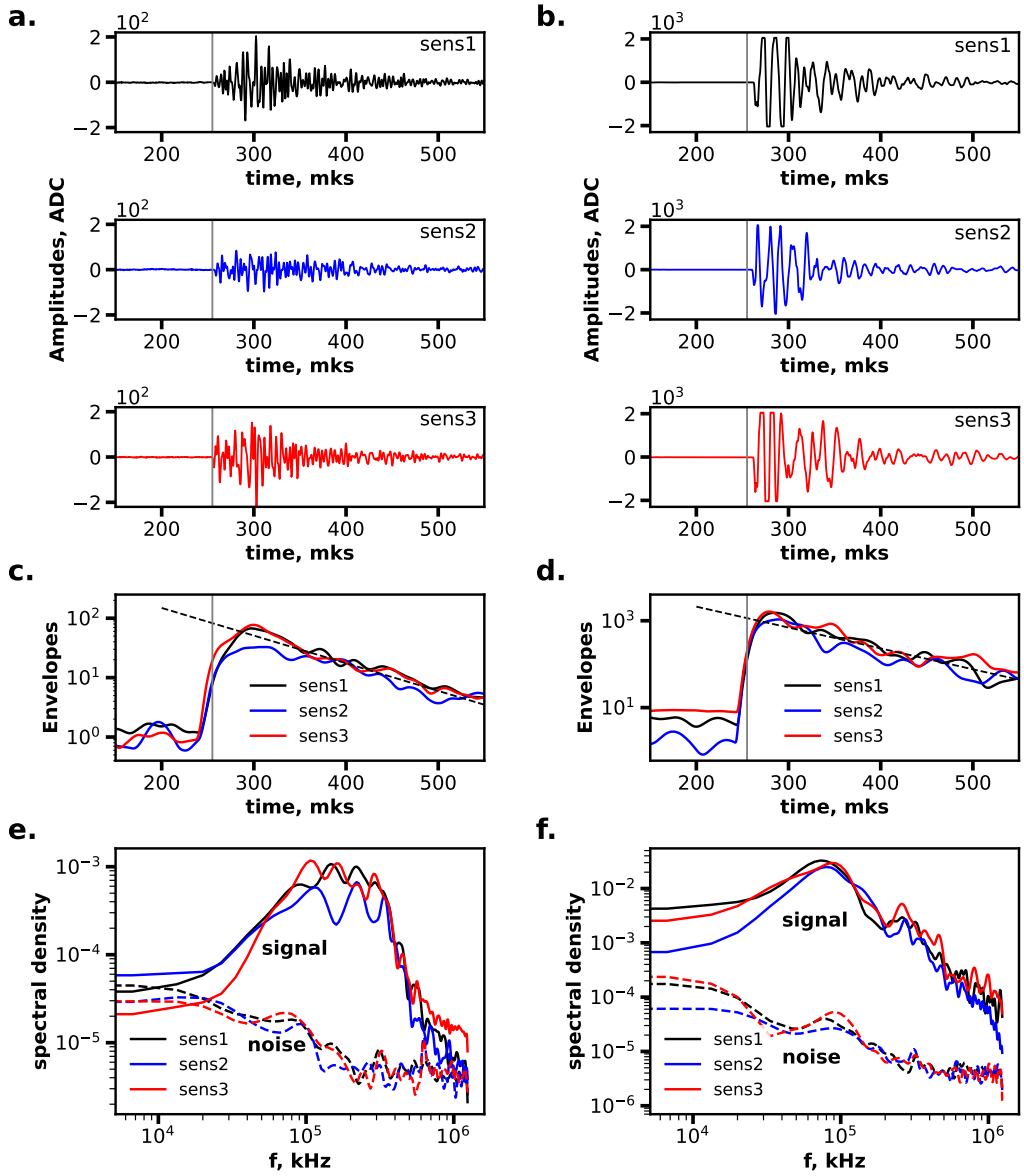

Figure 3. Examples of signals of a relatively weak (a) and a relatively strong (b) acoustic emission events. Recordings from sensors 1, 2 and 3 indicated in the bottom of Fig.1 are shown. Note the clipping of a signal amplitudes on (b). c) and d) Amplitude envelopes of records shown in (a) and (b) in the same color-code obtained by smoothing signal amplitudes with a 100 points long Hanning window ($40\mu s$). The dotted black lines indicate the linear approximation of coda parts ($320 - 500\mu s$) averaged over three sensors. Vertical lines mark the first arrival of event's signal ($255\mu s$). e) and f) Fourier amplitudes (same colors on (a) and (b)). Noise spectra (dotted curves) were calculated from $100 - 250\mu s$ windows. Signal spectra (solid curves) $250 - 400\mu s$ windows.

position (and ideally focal mechanism) to estimate the Green's function. For the AE events recorded during our laboratory experiments this approach is rather problematic because of the poor quality of the direct wave signals mentioned in the previous section and also because of unknown source locations for many of them.

To mitigate this problems, we use an approach that is based on the coda of the signal (e.g., Rautian & Khalturin, 1978; Mayeda & Walter, 1996; Sens-Schönfelder & Wegler, 2006). In seismology, the coda is formed by the waves scattered on the heterogeneities of the lithosphere (e.g., Aki & Chouet, 1975; Sato et al., 2012). The scattering is considered as a random processes leading to a formulation when the energy of wavefield is described with a radiative transfer theory (e.g., Margerin et al., 1998; Margerin, 2005). Based on this, a practical solution for a coda can be obtained when re-writing equations (7 and 8) and expressing the Green's functions in terms of energy. For observations this implies that we do not predict the whole signal (including its phase) but rather its envelope. When considering the scattering within the Earth's lithosphere the time dependence of the coda envelope can be approximated with a combination of an exponent and a power-low decays.

In the laboratory experiments, the geometry of coda formation is different comparing to the Earth's lithosphere. Instead of an infinite half-space the waves propagate within a small sample and are very quickly reflected at its boundaries. The coda is mostly formed by these multiply reflected waves. This reverberation is randomised because of the heterogeneities within the sample and on its boundaries. After a few reflections the wavefield can be approximated as diffuse with an energy nearly uniformly distributed over the sample (e.g., Weaver, 1984; Kanev, 2011). This is illustrated with an AE event shown in Fig. 3a and c when the amplitude of direct waves (arriving at $255 - 300\mu s$) can significantly differ from one sensor to another and becomes more homogeneous in the coda (after$\sim 320\mu s$). The energy is systematically lost at reflections and also due to the anelastic attenuation within the sample. As a result, its level decays exponentially in time (e.g., Farin et al., 2016) as illustrated with dashed lines in Fig. 3c and d. The energy decay rate considerably depends on frequency with high frequency waves attenuating faster. This is again illustrated in comparing envelopes in Fig. 3c and d. For a weaker event (c) whose spectrum contains more high frequencies, the coda amplitudes decay faster than for larger event shown in (d) with more low frequencies. Finally, the coda can be better described with an energy (or amplitude) envelope computed after applying a narrow-band filter. In this case, equations (7 and 8) can be rewritten as:

$$a_i^j(f,t) = a_0\, S_i(f)\, e^{-\alpha(f)\,(t-t_i)}\, R_j(f) \tag{9}$$

where t is time, $a_i^j(f,t)$ is the coda amplitude envelope computed from a signal recorded at receiver j during event i and bandpassed around frequency (f). a_0 is a factor depending on the experiment geometry. $\alpha(f)$ is the frequency dependent coda decay rate. As described in the following section, we use the system of equations (9) to retrieve the source spectra $S_i(f)$ (in a relative sense) from records of many events by multiple sensors. For this goal, the equations are linearized by taking their logarithms. Then, the idea is to compute the bandpassed envelopes from observed signals and to fit parameters of the model (9) in a least-squares sense. As described in the following section, this approach can be used to estimate the source spectral ratios. The last step, is to fit these estimations with a theoretical source model to extract corner frequencies and relative seismic moments.

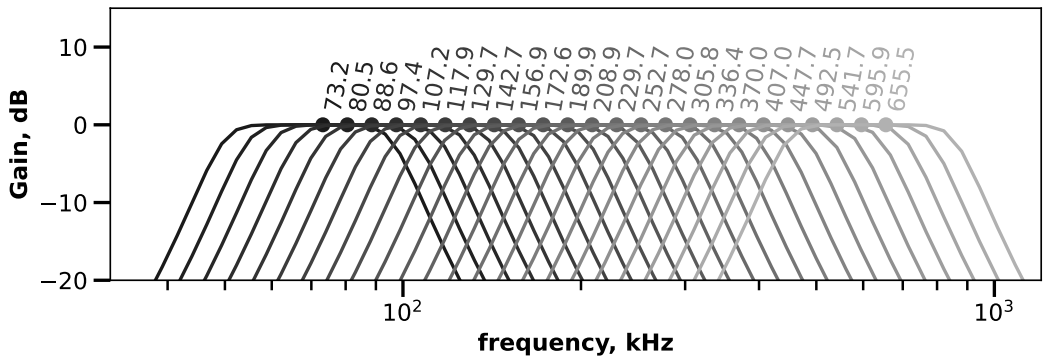

Figure 4. Amplitude responses of set of narrow-band Butterworth filters of 4th order used in this study. Corresponding central frequencies f_0 are noted above. Upper and lower cut-off frequencies of the filters (at $-3dB$ level) calculated as $f_0 - f_0/3$ and $f_0 + f_0/3$. The sequence of central frequencies is produced as $f_0^i = 1.1 \cdot f_0^{i-1}$

5 Methods

5.1 Computing Amplitude Envelopes

We start with applying to signals a set of narrow-band Butterworth filters of 4th order whose amplitude responses are shown on Fig. 4. Envelopes (amplitudes of Hilbert transforms) of all bandpassed signals are then smoothed with a 100 points long Hanning window ($40\mu s$). Examples of envelopes are shown in Fig. 5.

5.2 Selecting the Coda Window

The triggered recording system is set up in a such way that $255\mu s$ before each AE event are kept in memory implying that starting event time in every window is $255\mu s$. We consider that an average of $5-10$ reflections after first arrival are needed to form a diffuse coda, which gives the coda beginning time at $320\mu s$.

The end of the coda depends on the magnitude of the event and frequency range Fig. 5b. In order to save a sufficient amount of information for a stable analysis, while not allowing distortion of the estimates of the coda parameters due to capturing a section with noise, we adopt a simple approach to use a constant window with length of $50\mu s$ for all events and frequency ranges (as indicated with the shaded area in Fig. 5).

5.3 Estimating Coda Decay Together with Source and Receive Factors

The computed coda envelopes at every frequency f $a_i^j(f, t_k)$ (where t_k are time samples within the selected coda window) are fit to model (9) in order to estimate coda decay together with source and receiver factors. After taking logarithm this gives:

$$\lg a_i^j(f, t_k) = B_i(f) - \alpha(f) \lg e\, t_k + C_j(f) \tag{10}$$

where $B_i(f) = \lg S_i(f) + C_0(f)$, $C_j(f) = \lg R_j(f) + \lg a_0 + \alpha(f) \lg e\, t_i - C_0(f)$, and $C_0(f)$ is an arbitrary constant.

If we jointly consider N events recorded by M sensors, (10) gives us at every frequency a system of $N \times M \times K$ equation, with $N + M + 1$ unknowns. However, it remains degenerated because the unknowns B and C cannot be defined separately until

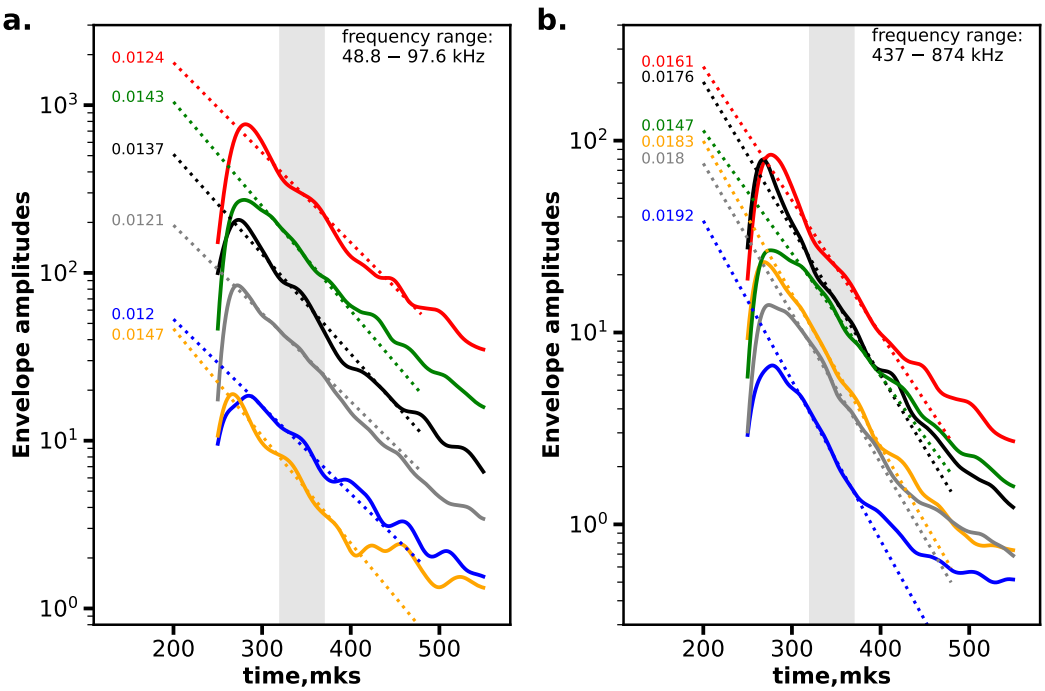

Figure 5. Coda amplitude envelopes of several events (from Stage I of Granite experiment) averaged over 16 sensors and their linear approximations: pre-filtered in $48.8 - 97.6\,kHz$ (a), $437 - 874\,kHz$ (b). Red curves correspond to the larger event from Fig. 3 and blue ones to smaller. Gray area marks the segment of the envelopes chosen for linear approximations. Corresponding $\alpha_i(f)$ (Fig. 9) posed near each line.

the constant C_0 is not fixed. Therefore, to stabilize the system of equations we add a "normalization" condition:

$$\sum_{j=1}^{M} C_j(f) = 0 \tag{11}$$

After introducing this additional condition, we solve system (10) in a least-squares sense to find the coda decay rate $\alpha(f)$ and the relative source and sensor factors $B_i(f)$ and $C_j(f)$.

5.4 Estimation of Corner Frequencies and Relative Seismic Moments

The estimated source parameters $B_i(f)$ cannot be directly used to estimate the absolute source spectra because of the coefficient $C_0(f)$ that is defined independently at each frequency. However, differences between $B_i(f)$ determined for different events is directly related to the source spectra ratios $SR_{i,j}(f)$ (e.g., Rautian & Khalturin, 1978):

$$SR_{i,j}(f) = 10^{(B_i(f)-B_j(f))} = \frac{S_i(f)}{S_j(f)} \tag{12}$$

We then use a theoretical source model to fit the observed spectral ratios and to estimate main source parameters. The simplest Brune's function (Brune, 1970) appeared not to be a best description of the observed spectral ratios since the degree of spectrum decay at frequencies above f_c is higher than 2. In our analysis, we prefer the Boatwright's model (e.g., Boatwright, 1980; Abercrombie, 1995; Ross & Ben-Zion, 2016)) in the form:

$$S(f) = \frac{C\,M_0}{\left(1 + \left(\frac{f}{f_c}\right)^{\gamma n}\right)^{1/\gamma}} \tag{13}$$

where M_0 is the seismic moment, f_c is the corner frequency, C is a normalisation coefficient, and γ and n are constants describing the spectral fall-off. In our case, the values $\gamma = 2$, $n = 3$ were found to better fit the observations. Deviations from $n = 2$ model have been also observed for earthquakes (Uchide & Imanishi, 2016; Eulenfeld & Wegler, 2016; Eulenfeld et al., 2022). Theoretical expression for the spectral ratio between sources i and j becomes:

$$\frac{S_i(f)}{S_j(f)} = dM_0^{ij} \left(\frac{1 + \left(\frac{f}{f_c^j}\right)^{\gamma n}}{1 + \left(\frac{f}{f_c^i}\right)^{\gamma n}} \right)^{\frac{1}{\gamma}} \tag{14}$$

where $dM_0^{ij} = M_0^i / M_0^j$ is the relative seismic moment.

In a next step, we use non-linear least-squares fitting implemented in a function "CurveFit" of "Optimize" package of "SciPy" library (Virtanen et al., 2020) to find parameters (f_c^i, f_c^j, and dM_0^{ij}) of this theoretical model that better fit the observed spectral ratios (12). An example is shown in Fig. 6.

5.5 Routine Analyses of Spectral Ratios

During the experiments lasting around several hours, and, depending on the loading program, signals of tens of thousands of AE events from 16 sensors were recorded.

Feeding all this data simultaneously into the system of equations Fig. 10 is not computationally optimal. More importantly, these equations are valid only when the coda decay rates $\alpha(f)$ and the sensor coefficients $R(f)$ remain constant for all considered AE events. This condition, however, cannot be fulfilled during the whole experiment during which the rock samples become strongly damaged and fractured resulting in significant variations of α. Also, strong variations of the confining pressure and loading stresses can modify the coupling between the sensors and the sample resulting in varying effective sensor responses. Therefore, we decided to process the event by relatively small groups ($N = 100$) corresponding to short time intervals during which α and R can be considered as constant.

After selecting a group of $N = 100$ events and estimating $B_i(f)$, they are sorted in descending order using $B_i(117\,kHz)$ as a scale since this characteristic is closer to the seismic moment estimated at low-frequencies. Then the spectral ratios are calculated for all possible pairs larger and smaller events that we call 'target' and 'eGf' (empirical Green's function), respectively. Then these 'target-eGf' spectral ratios are fitted with Fig. 14 to obtain estimates of relative seismic moments and respective corner frequencies. These estimates are considered stable only for pairs with spectral ratio increasing toward low frequencies and satisfying two following conditions: $\lg(f_c^{eGf}) - \lg(f_c^{target}) \geq 0.05$ and $dM_0^{target,eGf} > 1.2$.

Finally, each event of the group is involved in several 'target-eGf' pairs resulting in multiple estimations of its seismic moment relative to other event and of its corner frequency. We then analyse this ensemble of estimations statistically to define a most likely values of these parameters.

From all corner frequencies available for a given event, from both the target and eGf roles the median of the f_c distribution calculated as approximation of the true corner frequency (Fig. 6). The errors are estimated as 95% confidence interval with lower bound calculated as quantile cutting 2.5% of f_c distribution and the upper bound as quantile cutting 97.5%.

Ensemble of estimations of relative seismic moments gives a system of equations:

$$\lg dM_0^{ij} = \lg M_0^i - \lg M_0^j \tag{15}$$

The number of equations in this system is equal to number of spectral ratios which is larger than the number of unknown $\lg M_0^i$ (number of events, $N = 100$ in our case). Therefore, this systems can be solved in a least-squares sense. However, this system of equation only include differences between logarithms of moments and, therefore, requires an additional normalization condition to be solved. Finally, only relative values of seismic moments for the considered group of AE events are obtained.

Therefore, when processing many groups of events we need to make them overlap to end up with comparable values of seismic moments for the whole ensemble of analyzed event. We use groups with a 50% overlapping. The re-normalization of seismic moments in every new group is made based on the values estimated for 50 overlapping events estimated in the previous group. The first group is normalized by subtracting the minimal resulting $\lg M_0^k$.

We compute a mean difference between logarithms of moments for $N/2$ events present both in group I (earlier in experiment) and group II (later in experiment):

$$\overline{\Delta\ \lg(M_0)} = \frac{1}{N/2} \sum_{k=1}^{N/2} \left(\lg(M_0^k)_{II} - \lg(M_0^{k+N/2})_I \right) \tag{16}$$

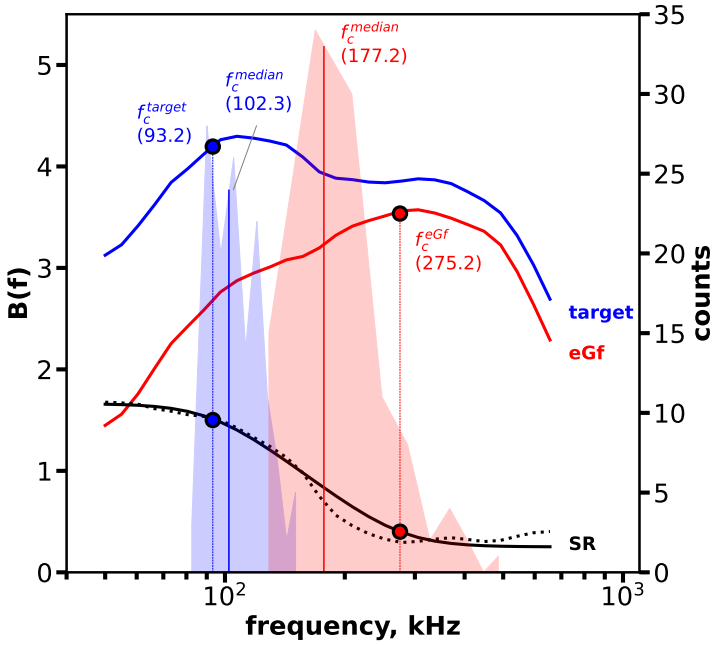

Figure 6. *Left axis:* spectra $B(f)$ and spectral ratio of two events from Fig. 3 (large-target in blue line, small-eGf in red line, their spectral ratio SR in doted black line). Boatwright approximation of spectral ratio ($\gamma = 2$, $n = 3$) is in black solid line. *Right axis:* corner frequency histograms for these events obtained from many spectral ratio pairs. Blue and red circles on SR and both $B(f)$ spectra curves mark estimated corner frequencies, corresponding vertical lines mark positions of these particular estimations in the resulting histograms. Solid vertical lines on histograms indicate the medians that are accepted as the best estimations of corner frequencies for both events.

Then, all seismic moments of group II are recalculated according to this correction:

$$\lg(M_0^i)'_{II} = \lg(M_0^i)_{II} + \overline{\Delta \lg(M_0)}, \tag{17}$$

Finally, for the $N/2$ overlapping events we recalculate seismic moments as average from two estimations:

$$\lg(M_0^k)'' = 1/2(\lg(M_0^k)'_{II} + \lg(M_0^{k+N/2})_I) \tag{18}$$

where k varies from 1 to $N/2$.

For the corner frequencies the values of the overlapping events are also modified. The median and corresponding quantiles are recalculated with accounting for the new f_c statistics coming from the group II.

5.6 Quality Control and Event Selection

At different steps of the analysis described above, several criteria of events selection are applied resulting in reduction of the final amount of AE-events with estimated source parameters:

1. Preliminary rejection of weak signals (average coda envelope amplitude at $320mks$ less then $300ADC$
2. During the short period $5404-5415s$ of Sandstone experiment 100 events were removed from the analyses since there were many overlapping waveforms because of fast development of the macro-fault
3. On the stage of spectral ratio parameters f_C^i, f_c^j and dM_0^{ij} estimation there imposed several criteria for selection of good pairs of events: (i) $dM_0^{ij} > \frac{S_i(2f_c^j)}{S_j(2f_c^j)}$ (see 14), (ii) $\lg(f_c^j) - \lg(f_c^i) \geq 0.05$, (iii) $dM_0^{ij} > 1.2$, where index i is responsible for 'target' event and j for 'eGf'. The condition (i) roughly checks the spectrum shape and for the best performance of spectral ratio method the difference between corner frequencies and their magnitudes of events are imposed via (ii) and (iii).
4. For statistical significance of the final estimation we consider events for which the amount of successful spectral ratios (that passed condition (3)) is larger than 20

While applying first two criteria rejected 19% in Granite experiment and 31% in Sandstone experiment, the third and forth ones reduced for other 25% and 36%, respectively. Finally, we kept 56% of AE events for Granite and 33% for Sandstone.

6 Results

After analyses of all records in both experiments and all applied criteria of selection there left: 20372 (56%) events in Granite experiment, 17638 (33%) events in Sandstone experiment. The general difference in amount of events left in analyses mainly caused by the preliminary massive rejection of weak signals. In the sandstone sample the relation of small events to large is higher than in the granite.

Fig. 7 a and g show the results for AE events recorded during the Stage I. During initial $\sim 900s$ of both experiments four steps of increasing isotropic confining pressure were applied to the samples. No macro-scale rock damage was observed in this period. It can be seen that during this stage most of events approximately align along a $f_c \sim M_0^{-1/3}$ scaling. Only for largest events we observe a "saturation" of corner frequencies at a level of $\sim 100kHz$. We also compute relative moment magnitudes (2 with

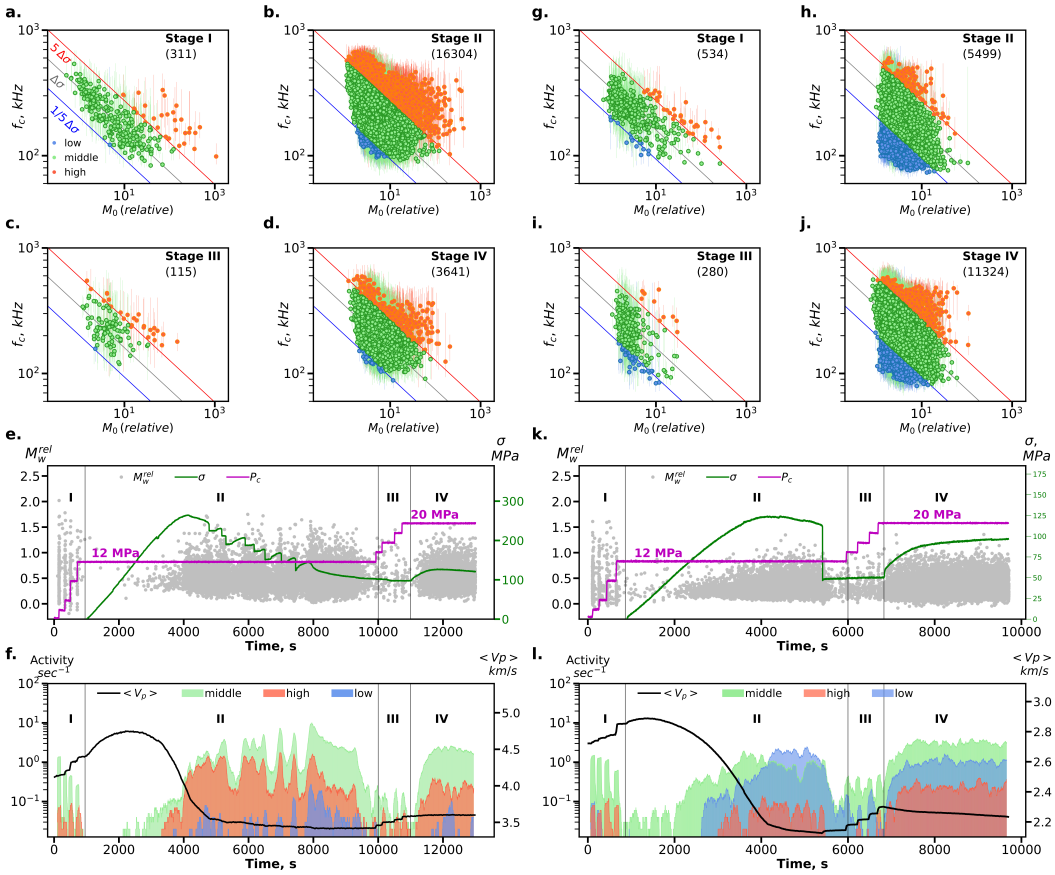

Figure 7. Results for Granite (left a-f), Sandstone (right g-l). Diagrams f_c *vs* M_0 for I-IV stages of Granite (a-d) and Sandstone (g-j): gray line - stress-drop reference ($f_c \sim M_0^{-1/3}$), blue and red - 5-fold decrease and increase of reference stress-drop respectively, numbers in brackets assign the ammount of events in current stage. Color of circles with error bars assigns position of point relative to stress-drop lines: $\leq 1/5\Delta\sigma$ - blue (low), between $1/5\Delta\sigma$ & $5\Delta\sigma$ - green (middle), $\geq 5\Delta\sigma$ - red (high). e) and k) *Left axis:* relative M_w (Fig. 2) - gray points. *Right axis:* differential stress σ - green curve. Confining pressure P_c - pink curve (more detailed on Fig. 2). f) and l) *Left axis:* activity (event/sec) of events with different stress-drops. Color of each barplot corresponds to the color of group on (a-d) and (g-j) panels. *Right axis:* black curves show averaged over 16 traces P-wave velocity changes.

$const = 0$) for these events and plot the magnitude frequency distribution in Fig. 8 with red lines. During the initial stages of both experiments (Granite and Sandstone) this distribution follow the power-law Gutenberg-Richter distribution with $b - value$ close to one. Overall, the behavior of AE events recorded during these first stages has strong similarities with the tectonic earthquakes and likely corresponds to rupturing pre-existing micro-fractures characterized by approximately constant stress drop. The level of this stress drop, however, cannot be established because of the lack of absolute values of seismic moments.

Several examples of eGf-corrected stacked spectra of target events from Stage I of both experiments are presented in Fig. 9. Each of these spectra S_i is obtained by stacking spectral ratios of given target i with the set of its best eGfs j normalized by the corresponding eGf's seismic moment $SR_{i,j}(f)M_0^j$ (equations 12, 14, 15). While four spec-

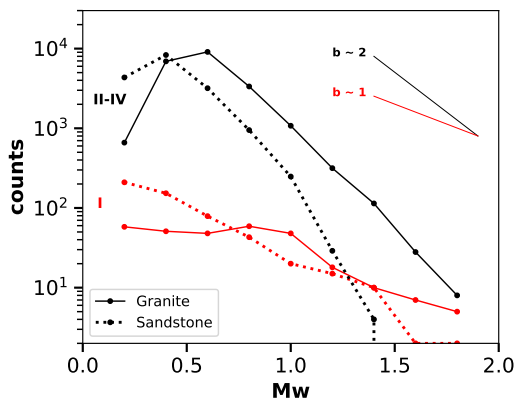

Figure 8. Gutenberg-Richter distributions of relative M_w for Granite (solid), Sandstone (dotted) on Stages I - in red, Stages II-IV in black. Lines in right-upper corner with different slopes ($b - values$) for comparison. Note that M_w are relative either between experiments.

tra of events lying close to the constant stress-drop line Fig. 9a demonstrate scaling similar to one described by (Aki, 1967), the other two events with higher corner frequencies (blue and orange) considerably deviate from this scaling.

For the interpretation of the AE emission recorded during all stages of the experiments, we set-up the position of the line $f_c = 70kHz \cdot \left(\frac{120}{M_0}\right)^{1/3}$ on log-log scale crossing the majority of events of Stage I (Fig. 7a, g, gray line), as a reference relative stress drop.

This level corresponds to initial conditions within the undamaged samples. Events significantly deviating from this line and lying above or below it are then considered to have larger or smaller stress drops, respectively.

Stages II of both experiments started with applying increasing axial load under constant confining pressure (Fig. 7e, k). This load gradually increases until the condition of formation of a macro-fracture of the samples are reached. This was followed by a decrease in the axial load, gradual in the case of granite and step-like in the case of sandstone. During stages III, the confining pressure is again increasing. Stages IV consist of additional increase of axial load under fixed confining pressure.

Two projections of AE-events locations on the Stages I and in the periods of $1000s$ after initiation of macro-faults being oriented concordantly with the photos of samples in copper jackets after tests, demonstrate difference between rock types as well Fig. 10. For the granite Fig. 10a event locations on the Stage I tend to orient along one direction while in the sandstone Fig. 10b locations from the first stage distributed around the whole volume of the sample and only after the failure events locations aligned in the plane of the slip.

After active fracturing during Stages II, the Stages III is designed to consolidate the sample by applying steps of confining pressure similar to that of Stages I but with the presence of non-changing axial load. The level of "stress-drop" during this stage is similar to Stages I with mopst of events concentrating around reference $\Delta\sigma$ (Fig. 7 c and i). However, these stages are depleted in large-scale events.

In contrast to the Stages I and III the estimations from the Stages II and IV demonstrate large diversity of stress-drops. If the gray line assigns the reference level of con-

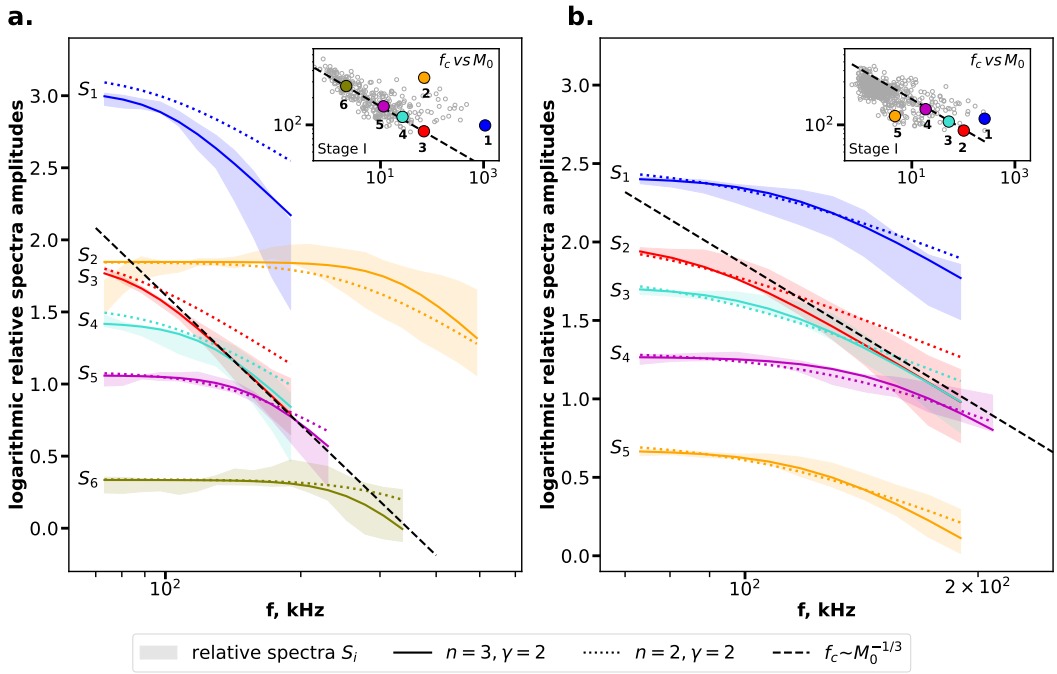

Figure 9. Examples of eGf-corrected normalized stacked spectra (eq.N) from Stage I of Granite (a) and Sandstone (b). The target events chosen for spectra demonstration are marked with colored points on the inserts showing Stage I diagrams identical to Fig. 7a, g. The number of each target event corresponds to the number of spectra $S_1 - S_6$ for granite and $S_1 - S_5$ for sandstone. The spectra bands S_i represent the variation of eGf corrected normalized spectra set for a given i^{th} target (around $5 - 10$ for each target). Because of specific procedure of estimation of final f_c and M_0 that is based on the set of parameters without strict separation of events on 'targets' and 'eGfs' and selection of successful spectral ratios (Fig. 5.6) the amount of appropriate pairs of chosen targets with their eGfs is quite small, especially, if demonstrating group of targets of equal stress-drop, i.e. following the same cubic line $f_c \sim M_0^{-1/3}$ (dached lines). Two spectra decay rate $n = 3$ and $n = 2$ of Boatwright model with $\gamma = 2$ also presented. While M_0^j of $n = 3$ model was used here for normalizing spectral ratios, it is seen that seismic moment estimations of both models are quite similar unlike the corner frequencies.

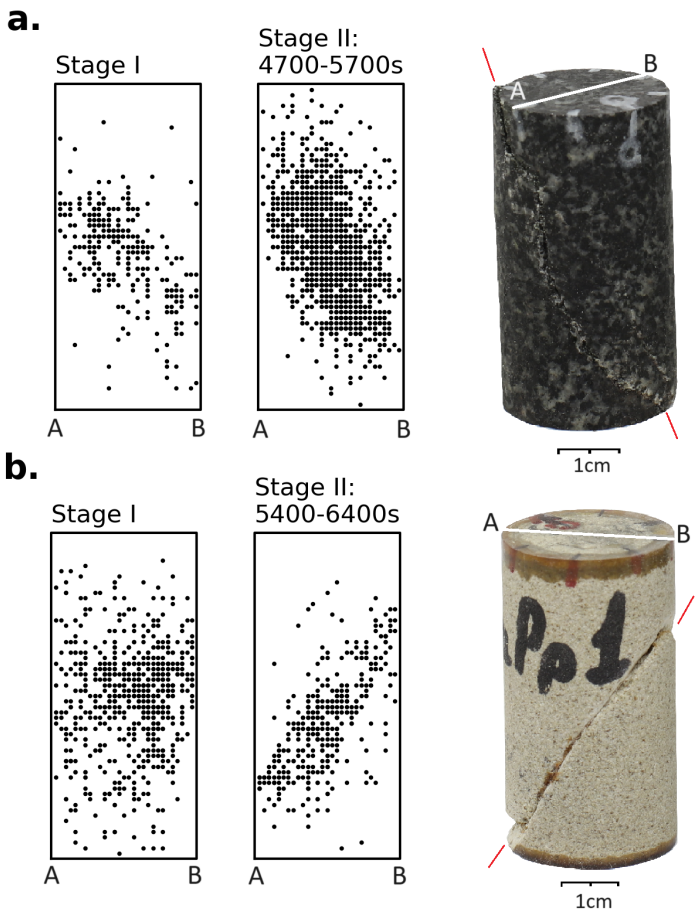

Figure 10. Location of AE-events with the photos of samples after experiments a - Granite and b - Sandstone: the periods from which locations (Fig. 3) were taken are marked above the corresponding panels. Orientation of macro-faults are marked by red arrows.

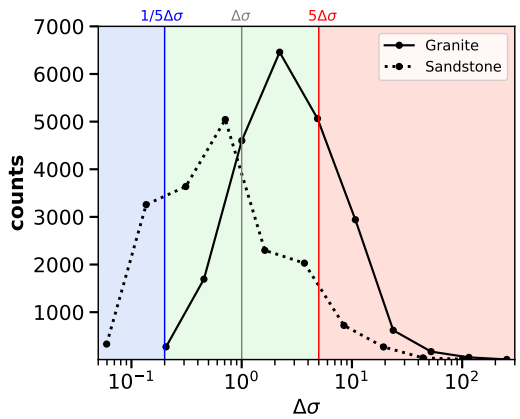

Figure 11. Distribution of apparent stress-drops in both experiments. Vertical lines correspond to that of the lines on Fig. 7a-d and g-j with colored area assigning the ranges of low (blue), middle (green) and high (red) stress-drops.

stant stress-drops $\Delta\sigma$ based on Stage I, the red and blue lines represent 5-fold increase and decrease in stress-drop, respectively. Statistical distribution compiled during all 4 stages (Fig. 11) demonstrate that in granite the overall stress-drop is higher than the initial reference level and inverse situation is observed in the sandstone sample.

The dynamics of stress-drops with highly variable experimental conditions is shown in Fig. 7f, l with color of each bar-plot linked to the corresponding group of events in Fig. 7a-d, g-j. Above mentioned balance between high and low stress drop events in both experiments is clearly observed with some details in temporal variability that can reflect the internal changes during fracturing process (Fig. 7f and l). In the Granite experiment, initiation of damage and formation of the micro-fracture is associated with appearance of many "high stress drop" events that remain nearly dominating (with numbers very close to "normal stress drop" events) till the axial load is reduced to the pre-fracture level (at $\sim 8000s$). In the sandstone, the initiation of damage at $\sim 3000s$ is associated with the "low stress drop" events that persist till the release of the axial load at $\sim 6000s$ and then re-appear in stage IV when the axial load is increased again. We note, that this kind of dynamics that could not be retrieved from "standard" analyses based on occurrence times and magnitudes.

The Gutenberg-Richter distributions obtained during Stages II-IV in granite and sandstone are shown in Fig. 8 with black solid and dashed lines, respectively, have much higher $b-values$. The magnitudes of completeness are higher than during Stage I, which is explained by the selection criteria imposed on the f_c differences in spectral ratios (Section "5.5 Routine analyses of spectral ratios") and less amount of events satisfying these criteria particularly on Stages II. Nevertheless, the *b-values* observed during these later stages are significantly higher than 1.

7 Discussion and Conclusions

In this paper we described a new approach to estimate the relative source spectra of AE events from codas of signals recorded during laboratory experiments. The respective spectral ratios can be used to estimate main source parameters: corner frequencies f_c and relative seismic moment M_0. The decay of the coda amplitude envelopes is described with a simple diffuse approximation (e.g., Farin et al., 2016). In small samples, the diffuse wavefield is mainly formed by multiple reverberations leading to a nearly ho-

mogeneous distribution of energy across the media. This implies equal amplitude level and decay rate at all sensors, independent of their position and the source location and mechanism. Overall, the proposed coda based source spectra estimation have an advantage of being relatively simple, i.e., it does not require information about the source locations and mechanisms, separation of direct P and S waves, and well calibrated acoustic recording system. Therefore, it can be potentially applied to many experiments run on relatively small rock samples.

We validated the developed method by applying to AE signals recorded during two experiments described in Section "3 Data". With the selected data quality criteria (Section "5.6 Quality Control and Event Selection") we could determine the relative seismic moments and corner frequencies for 30−60% of all recorded AE events. As a main result, the AE catalogues were enriched with two new physical parameters whose evolution as function of loading conditions could be studied.

We were particularly interested in verifying if the recorded AE events followed a behaviour similar to regular earthquakes that are known to exhibit nearly constant stress-drop independent of their size and to obey a Gutenberg-Richter law with *b-values* close to 1. For this goal, we investigated two observable relationships: (1) the scaling between the seismic moment and the corner frequency, and (2) the Gutenberg-Richter distribution computed from moment magnitudes M_W. In the "regular earthquake regime", the scaling is expected to be cubic (equation 6) and the *b-value* being close to one.

We have found that two above mentioned attributes of the "regular earthquake regime" have been approximately verified during initial stages of both experiments when the rock samples were loaded with increasing isotropic confining pressure. The origin of the AE during this stage is most likely related to the inhomogeneity of the rock samples that results in a heterogeneous internal stress distributions even under an isotropic loading. The AE events can be triggered at the stress concentrators such as preexisting micro-faults, pores or grain boundaries having high contrast in physical properties (Anders et al., 2014). The observed similarity with natural earthquakes can be interpreted that these Stage I AE events mostly occur on preexisting micro faults with a nearly constant stress drop. Existence of such preexisting micro faults is partially confirmed by the distribution of AE hypocenters from the experiment in granite (Fig. 10a) that start to be aligned even during Stage I.

The behavior of the AE events changes drastically once the samples become significantly damaged and many new micro fractures start to appear under the axial load (Stages II and IV). The dots on the log-log f_c−M_0 plane do not align along a line (Fig. 7b and d, h and g but form a "cloud" with appearance of many events whose spectra are either enriched or depleted in high frequencies comparing to the "reference" level observed during Stage I. The *b-value* of the Gutenberg-Richter distribution becomes much larger than 1 (Fig. 8 black curves). One possible hypotheses for explaining this is that the *b-value* can be related to the level of stress (e.g., Main et al., 1989; V. B. Smirnov et al., 2019; V. Smirnov & Ponomarev, 2020; Dong et al., 2022).

Overall, the behavior observed during Stages II and IV is very different from the "regular earthquake regime". One important implication of this result is that a direct comparison of laboratory and natural earthquakes is not always appropriate and that in some laboratory regimes, e.g., associated with active sample damage, the mechanisms of rock deformation faulting might be very different from natural conditions in the Earth's lithosphere.

Additionally, we observe different behaviors in the experiments performed on different rocks. From the granite experiment we retrieve more events enriched in high frequencies during Stages II and IV (red area in Fig. 7f), the activity shifts toward events depleted in high frequencies (red area in Fig. 7l) in the sandstone sample. One possi-

bility is to interpret the observed distributions in the $f_c - M_0$ plane in terms of varying stress-drop. Events enriched and depleted in high frequencies (red and blue colors in Fig. 7a-d, g-j) would be associated with the increased and reduced levels of stress-drop, respectively. The increased stress drop events might be associated with creation of new micro faults. The low stress drop level might be associated with re-activation of recently opened fractures or other types of "weak" contacts in the rock. The latter are more likely to be present in the more porous sandstone which could explain the larger relative number of events depleted in high frequencies recorded during this experiment.

However, the concept of "stress-drop" should be applied to our results with a certain caution. The stress-drop expressed through the seismic moment and corner frequency scaling results from the ideal earthquake source model that considers the faults with constant rupture propagation speed. The faulting mechanisms within the actively damaged rock samples can be far from this idealisation.

One important limitation of the results obtained in this study is that absolute values of source parameters could not be estimated. This first concerns the seismic moments. Without knowing their relative values, the $M_0 - f_c$ scaling can be estimated only within the range of measured corner frequencies. However, it cannot be compared with more global trends (e.g., Goodfellow & Young, 2014; Yoshimitsu et al., 2014). To advance in this direction we would need to estimate absolute values of seismic moments for at least a few AE events. This could be eventually achieved with an improved calibration of the recording acoustic system.

Another difficulty is to estimate the spatial extension of the AE event sources. Following the "standard" earthquake model they can be related to corner frequencies as: $L \approx V_r/f_c$. For real earthquakes the rupture speed V_r is known to be close to the shear wave speed, i.e., of the order of a few kilometers per second. Applying this to our data would give source dimensions between millimeters and centimeters. In particular, the source dimensions corresponding to largest observed corner frequencies ($70-100kHz$) would be close to the sample size. This could explain the observed "saturation" at low corner frequencies. At the same time, we cannot fully exclude a possibility that this saturation is caused by poor response of the acoustic recording system at low frequencies. More importantly, the millimetric to centimetric source sizes do not match the dimensions of micro-fractures measured in samples that are usually nucleated and associated to the grain boundaries and therefore do not exceed the average grain size (Anders et al. (2014) 3.2, 3.3 for a review) that in the case of Berea sandstone not larger than $0.3-0.5$, and granite of Voronezh massif $1-2mm$. This discrepancy could be another indication of the difference between the natural tectonic earthquakes and the fracturing and damaging of the small laboratory rock samples.

Overall, the use of coda waves in the solving the problem of laboratory AE-source characterization seems to be promising. It can become a useful tool to enrich the knowledge about the fracture process.

8 Open Research

The numerical data containing raw AE-waveform records, appearance of AE-events in time, loading curves and results (absolute corner frequencies, relative seismic moments and relative stress-drops) used and obtained in this study are available at Zenodo via (T. Kartseva, 2023) with open access.

Acknowledgments

This study was supported by the European Research Council under the European Union Horizon 2020 research and innovation program (Grant Agreement 787399-SEISMAZE)

and by the Russian Ministry of Education and Science (Grant 14.W03.31.0033 "Geophysical research, monitoring and forecasting of catastrophic geodynamic processes in the Russian Far East"). Experiments carried out in the RESC of IPE RAS "Petrophysics, Geomechanics and Paleomagnetism" on a controlled hydraulic press INOVA-1000 of the Geophysical Observatory"Borok", IPE RAS.

We want to thank all co-authors for their contribution to this article:

Tatiana I. Kartseva: conceived and designed the experiment and analyses, contributed data analyses and tools, wrote the paper

Nikolai M. Shapiro: conceived and designed the analyses, contributed data analyses and tools, reviewed the paper, provided funding of the project

Andrey V. Patonin: conducted experiments and preliminary data analyses, participated in discussion of research progress, reviewed the paper

Natalia M. Shikhova: conducted experiments and preliminary data analyses, participated in discussion of research progress, reviewed the paper

Vladimir. B. Smirnov: conceived and designed the experiment, participated in discussion of research progress, provided financial and material support of laboratory, reviewed the paper

Alexander V. Ponomarev: conceived and designed the experiment, provided financial and material support of laboratory, reviewed the paper

References

Abercrombie, R. E. (1995). Earthquake source scaling relationships from- 1 to 5 ml using seismograms recorded at 2.5-km depth. *Journal of Geophysical Research: Solid Earth*, *100*(B12), 24015–24036.

Aki, K. (1966). Generation and propagation of g waves from the niigata earthquake of june 16, 1964. : Part 2. estimation of earthquake moment, released energy, and stress-strain drop from the g wave spectrum. *Bulletin of the Earthquake Research Institute*, *44*(1), 73–88.

Aki, K. (1967). Scaling law of seismic spectrum. *Journal of geophysical research*, *72*(4), 1217–1231.

Aki, K., & Chouet, B. (1975, aug). Origin of coda waves: Source, attenuation, and scattering effects. *Journal of Geophysical Research*, *80*(23), 3322–3342. doi: 10.1029/jb080i023p03322

Allmann, B. P., & Shearer, P. M. (2009, jan 23). Global variations of stress drop for moderate to large earthquakes. *Journal of Geophysical Research: Solid Earth*, *114*(B1). doi: 10.1029/2008jb005821

Anders, M. H., Laubach, S. E., & Scholz, C. H. (2014). Microfractures: A review. *Journal of Structural Geology*, *69*, 377–394.

Båth, M. (1966). Earthquake energy and magnitude. *Physics and Chemistry of the Earth*, *7*, 115-165. doi: https://doi.org/10.1016/0079-1946(66)90003-6

Blanke, A., Kwiatek, G., Goebel, T. H. W., Bohnhoff, M., & Dresen, G. (2020, nov 3). Stress drop magnitude dependence of acoustic emissions during laboratory stick-slip. *Geophysical Journal International*, *224*(2), 1371–1380. doi: 10.1093/gji/ggaa524

Boatwright, J. (1980, 02). A spectral theory for circular seismic sources; simple estimates of source dimension, dynamic stress drop, and radiated seismic energy. *Bulletin of the Seismological Society of America*, *70*(1), 1-27. doi: 10.1785/BSSA0700010001

Bolton, D. C., Marone, C., Saffer, D., & Trugman, D. T. (2023). Foreshock prop-

erties illuminate nucleation processes of slow and fast laboratory earthquakes. *Nature Communications*, *14*(1), 3859.

Bostock, M. G., Thomas, A. M., Savard, G., Chuang, L., & Rubin, A. M. (2015). Magnitudes and moment-duration scaling of low-frequency earthquakes beneath southern vancouver island. *Journal of Geophysical Research: Solid Earth*, *120*(9), 6329-6350. doi: https://doi.org/10.1002/2015JB012195

Brune, J. (1970). Tectonic stress and the spectra of seismic shear waves from earthquakes..

Dong, L., Zhang, L., Liu, H., Du, K., & Liu, X. (2022). Acoustic emission b value characteristics of granite under true triaxial stress. *Mathematics*, *10*(3). Retrieved from `https://www.mdpi.com/2227-7390/10/3/451` doi: 10.3390/math10030451

Eulenfeld, T., Dahm, T., Heimann, S., & Wegler, U. (2022). Fast and robust earthquake source spectra and moment magnitudes from envelope inversion. *Bulletin of the Seismological Society of America*, *112*(2), 878–893.

Eulenfeld, T., & Wegler, U. (2016). Measurement of intrinsic and scattering attenuation of shear waves in two sedimentary basins and comparison to crystalline sites in germany. *Geophysical Journal International*, *205*(2), 744–757.

Farge, G., Shapiro, N. M., & Frank, W. B. (2020). Moment-duration scaling of low-frequency earthquakes in guerrero, mexico. *Journal of Geophysical Research: Solid Earth*, *125*(8), e2019JB019099.

Farin, M., Mangeney, A., de Rosny, J., Toussaint, R., Sainte-Marie, J., & Shapiro, N. M. (2016, feb 4). Experimental validation of theoretical methods to estimate the energy radiated by elastic waves during an impact. *Journal of Sound and Vibration*, *362*, 176–202. doi: 10.1016/j.jsv.2015.10.003

Galina, N. A., Shapiro, N. M., Droznin, D. V., Droznina, S. Y., Senyukov, S. L., & Chebrov, D. V. (2020). Recurrence of deep long-period earthquakes beneath the klyuchevskoi volcano group, kamchatka. *Izvestiya, Physics of the Solid Earth*, *56*(6), 749–761. doi: 10.1134/S1069351320060026

Goodfellow, S. D., & Young, R. P. (2014). A laboratory acoustic emission experiment under in situ conditions. *Geophysical Research Letters*, *41*(10), 3422-3430. doi: https://doi.org/10.1002/2014GL059965

Gutenberg, B., & Richter, C. F. (1944, 10). Frequency of earthquakes in California*. *Bulletin of the Seismological Society of America*, *34*(4), 185-188. Retrieved from `https://doi.org/10.1785/BSSA0340040185` doi: 10.1785/BSSA0340040185

Hanks, T. C., & Kanamori, H. (1979). A moment magnitude scale. *Journal of Geophysical Research: Solid Earth*, *84*(B5), 2348-2350. doi: https://doi.org/10.1029/JB084iB05p02348

Harrington, R. M., & Benson, P. M. (2011, nov 9). Analysis of laboratory simulations of volcanic hybrid earthquakes using empirical green's functions. *Journal of Geophysical Research: Solid Earth*, *116*(B11). doi: 10.1029/2011jb008373

Haskell, N. A. (1964, 12). Total energy and energy spectral density of elastic wave radiation from propagating faults. *Bulletin of the Seismological Society of America*, *54*(6A), 1811-1841. doi: 10.1785/BSSA05406A1811

Ide, S., & Beroza, G. C. (2023). Slow earthquake scaling reconsidered as a boundary between distinct modes of rupture propagation. *Proceedings of the National Academy of Sciences*, *120*(32), e2222102120. doi: 10.1073/pnas.2222102120

Ide, S., Beroza, G. C., Shelly, D. R., & Uchide, T. (2007). A scaling law for slow earthquakes. *Nature*, *447*(7140), 76–79. doi: 10.1038/nature05780

Jacobs, K. M., & McNutt, S. R. (2010). *Using seismic b-values to interpret seismicity rates and physical processes during the preeruptive earthquake swarm at augustine volcano 2005-2006: Chapter 3 in the 2006 eruption of augustine volcano, alaska* (Tech. Rep.). US Geological Survey.

Kanamori, H., & Anderson, D. L. (1975, 10). Theoretical basis of some empirical re-

lations in seismology. *Bulletin of the Seismological Society of America*, *65*(5), 1073-1095. doi: 10.1785/BSSA0650051073

Kanev, N. (2011). Sound decay in a rectangular room with specular and diffuse reflecting surfaces..

Kartseva, T. (2023). *Acoustic data and loading regime of two rock physics experiments carried out on inova-1000 test-complex, borok, russia* [dataset]. Zenodo. Retrieved from `https://zenodo.org/records/10036388` doi: 10.5281/zenodo.10036388

Kartseva, T. I., Shapiro, N. M., Patonin, A. V., Smirnov, V. B., & Ponomarev, A. V. (2022, feb). Energy classification of acoustic events using the coda of a signal. *Seismic Instruments*, *58*(1), 18–25. doi: 10.3103/s0747923922010054

Kwiatek, G., Plenkers, K., & and, G. D. (2011, dec). Source parameters of picoseismicity recorded at mponeng deep gold mine, south africa: Implications for scaling relations. *Bulletin of the Seismological Society of America*, *101*(6), 2592–2608. doi: 10.1785/0120110094

Lengliné, O., Lamourette, L., Vivin, L., Cuenot, N., & Schmittbuhl, J. (2014). Fluid-induced earthquakes with variable stress drop. *Journal of Geophysical Research: Solid Earth*, *119*(12), 8900-8913. doi: https://doi.org/10.1002/2014JB011282

Lockner, D., Byerlee, J., Kuksenko, V., Ponomarev, A., & Sidorin, A. (1991). Quasi-static fault growth and shear fracture energy in granite. *Nature*, *350*(6313), 39–42.

Main, I. G., Meredith, P. G., & Jones, C. (1989). A reinterpretation of the precursory seismic b-value anomaly from fracture mechanics. *Geophysical Journal International*, *96*(1), 131–138.

Margerin, L. (2005). Introduction to radiative transfer of seismic waves. In *Seismic earth: Array analysis of broadband seismograms* (p. 229-252). American Geophysical Union (AGU). doi: https://doi.org/10.1029/157GM14

Margerin, L., Campillo, M., & Tiggelen, B. (1998, 08). Radiative transfer and diffusion of waves in a layered medium: new insight into coda Q. *Geophysical Journal International*, *134*(2), 596-612. doi: 10.1111/j.1365-246X.1998.tb07142.x

Marty, S., Schubnel, A., Bhat, H., Aubry, J., Fukuyama, E., Latour, S., ... Madariaga, R. (2023). Nucleation of laboratory earthquakes: Quantitative analysis and scalings. *Journal of Geophysical Research: Solid Earth*, *128*(3), e2022JB026294.

Mayeda, K., Malagnini, L., & Walter, W. R. (2007). A new spectral ratio method using narrow band coda envelopes: Evidence for non-self-similarity in the hector mine sequence. *Geophysical Research Letters*, *34*(11), L11303. doi: https://doi.org/10.1029/2007GL030041

Mayeda, K., & Walter, W. R. (1996). Moment, energy, stress drop, and source spectra of western united states earthquakes from regional coda envelopes. *Journal of Geophysical Research: Solid Earth*, *101*(B5), 11195-11208. doi: https://doi.org/10.1029/96JB00112

McLaskey, G. C., & Kilgore, B. D. (2013). Foreshocks during the nucleation of stick-slip instability. *Journal of Geophysical Research: Solid Earth*, *118*(6), 2982–2997.

McLaskey, G. C., & Lockner, D. A. (2016, sep). Calibrated acoustic emission system records m -3.5 to m -8 events generated on a saw-cut granite sample. *Rock Mechanics and Rock Engineering*, *49*(11), 4527–4536. doi: 10.1007/s00603-016-1082-1

Omori, F. (1894). n the aftershocks of earthquakes. *Journal of the College of Science, Imperial University of Tokyo*, *7*, 111–120.

Patonin, A., Ponomarev, A., & Smirnov, V. (2014). A laboratory instrumental complex for studying the physics of the destruction of rocks. *Seismic instruments*, *50*, 9–19.

Patonin, A. V., Shikhova, N. M., Ponomarev, A. V., & Smirnov, V. B. (2019, jun). A modular system for continuous recording of acoustic emission for laboratory studies of rock destruction processes. *Seismic Instruments*, *55*(3), 313–326. doi: 10.3103/s0747923919030101

Peng, Z., & Gomberg, J. (2010). An integrated perspective of the continuum between earthquakes and slow-slip phenomena. *Nature Geoscience*, *3*(9), 599–607. doi: 10.1038/ngeo940

Prieto, G. A., Shearer, P. M., Vernon, F. L., & Kilb, D. (2004, aug 28). Earthquake source scaling and self-similarity estimation from stacking spectra. *Journal of Geophysical Research: Solid Earth*, *109*(B8). doi: 10.1029/2004jb003084

Rautian, T., & Khalturin, V. (1978). The use of the coda for determination of the earthquake source spectrum. *Bulletin of the Seismological Society of America*, *68*(4), 923–948.

Ross, Z. E., & Ben-Zion, Y. (2016, jun). Toward reliable automated estimates of earthquake source properties from body wave spectra. *Journal of Geophysical Research: Solid Earth*, *121*(6), 4390–4407. doi: 10.1002/2016jb013003

Sato, H., Fehler, M., & Maeda, T. (2012). *Seismic wave propagation and scattering in the heterogeneous earth: Second edition*. Springer Berlin, Heidelberg. doi: 10.1007/978-3-642-23029-5

Schlische, R. W., Young, S. S., Ackermann, R. V., & Gupta, A. (1996, 08). Geometry and scaling relations of a population of very small rift-related normal faults. *Geology*, *24*(8), 683-686. doi: 10.1130/0091-7613(1996)024⟨0683:GASROA⟩2.3.CO;2

Scholz, C. H. (1968). Experimental study of the fracturing process in brittle rock. *Journal of Geophysical Research (1896-1977)*, *73*(4), 1447-1454. Retrieved from `https://agupubs.onlinelibrary.wiley.com/doi/abs/10.1029/JB073i004p01447` doi: https://doi.org/10.1029/JB073i004p01447

Sens-Schönfelder, C., & Wegler, U. (2006, 12). Radiative transfer theory for estimation of the seismic moment. *Geophysical Journal International*, *167*(3), 1363-1372. doi: 10.1111/j.1365-246X.2006.03139.x

Shapiro, S. A., & Dinske, C. (2021). Stress drop, seismogenic index and fault cohesion of fluid-induced earthquakes. *Rock Mechanics and Rock Engineering*, *54*(10), 5483–5492. doi: 10.1007/s00603-021-02420-3

Smirnov, V., & Ponomarev, A. (2020). *Physics of transient seismicity regimes (in russian)*. Russain Academy of Sciences.

Smirnov, V. B., Ponomarev, A. V., Stanchits, S. A., Potanina, M. G., Patonin, A. V., Dresen, G., ... Stroganova, S. M. (2019). Laboratory modeling of aftershock sequences: Stress dependences of the omori and gutenberg–richter parameters. *Izvestiya, Physics of the Solid Earth*, *55*(1), 124–137. doi: 10.1134/S1069351319010105

Supino, M., Poiata, N., Festa, G., Vilotte, J.-P., Satriano, C., & Obara, K. (2020). Self-similarity of low-frequency earthquakes. *Scientific reports*, *10*(1), 1–9.

Uchide, T., & Imanishi, K. (2016). Small earthquakes deviate from the omega-square model as revealed by multiple spectral ratio analysis. *Bulletin of the Seismological Society of America*, *106*(3), 1357–1363.

Virtanen, P., Gommers, R., Oliphant, T. E., Haberland, M., Reddy, T., Cournapeau, D., ... SciPy 1.0 Contributors (2020). SciPy 1.0: Fundamental Algorithms for Scientific Computing in Python. *Nature Methods*, *17*, 261–272. doi: 10.1038/s41592-019-0686-2

Weaver, R. (1984). Diffuse waves in finite plates..

Wu, Q., Chapman, M., & Chen, X. (2018, 05). Stress-Drop Variations of Induced Earthquakes in Oklahoma. *Bulletin of the Seismological Society of America*, *108*(3A), 1107-1123. doi: 10.1785/0120170335

Wyss, M., McNutt, S. R., & Wyss, M. (1998). Temporal and three-dimensional spatial analyses of the frequency–magnitude distribution near long valley caldera,

california. *Geophysical Journal International*, *134*(2), 409–421.

Yoshimitsu, N., Kawakata, H., & Takahashi, N. (2014, jul). Magnitude -7 level earthquakes: A new lower limit of self-similarity in seismic scaling relationships. *Geophysical Research Letters*, *41*(13), 4495–4502. doi: 10.1002/2014gl060306

Figure1.

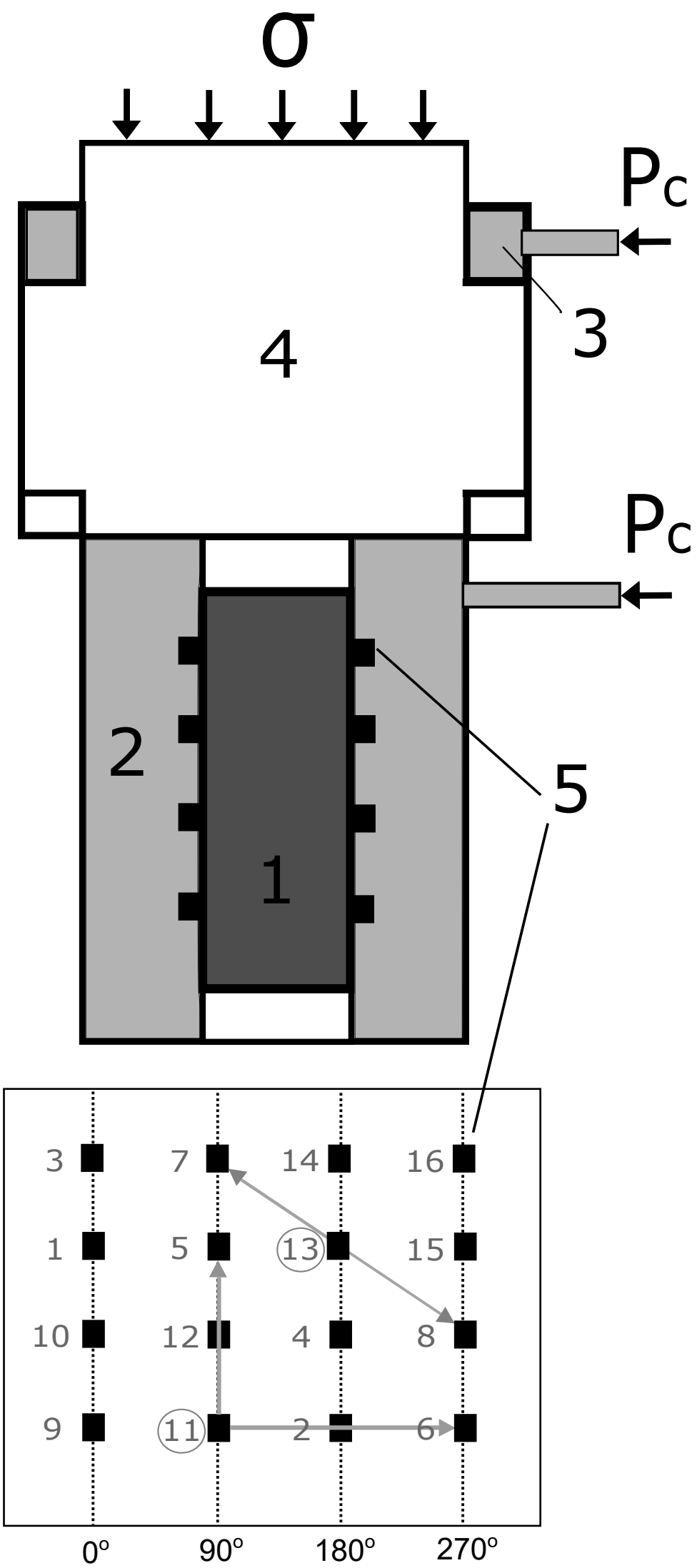
σ
Pc
3
4
Pc
2
5
1
3
7
14
16
1
5
13
15
10
12
4
8
9
11
2
6
0°
90°
180°
270°

Figure2.

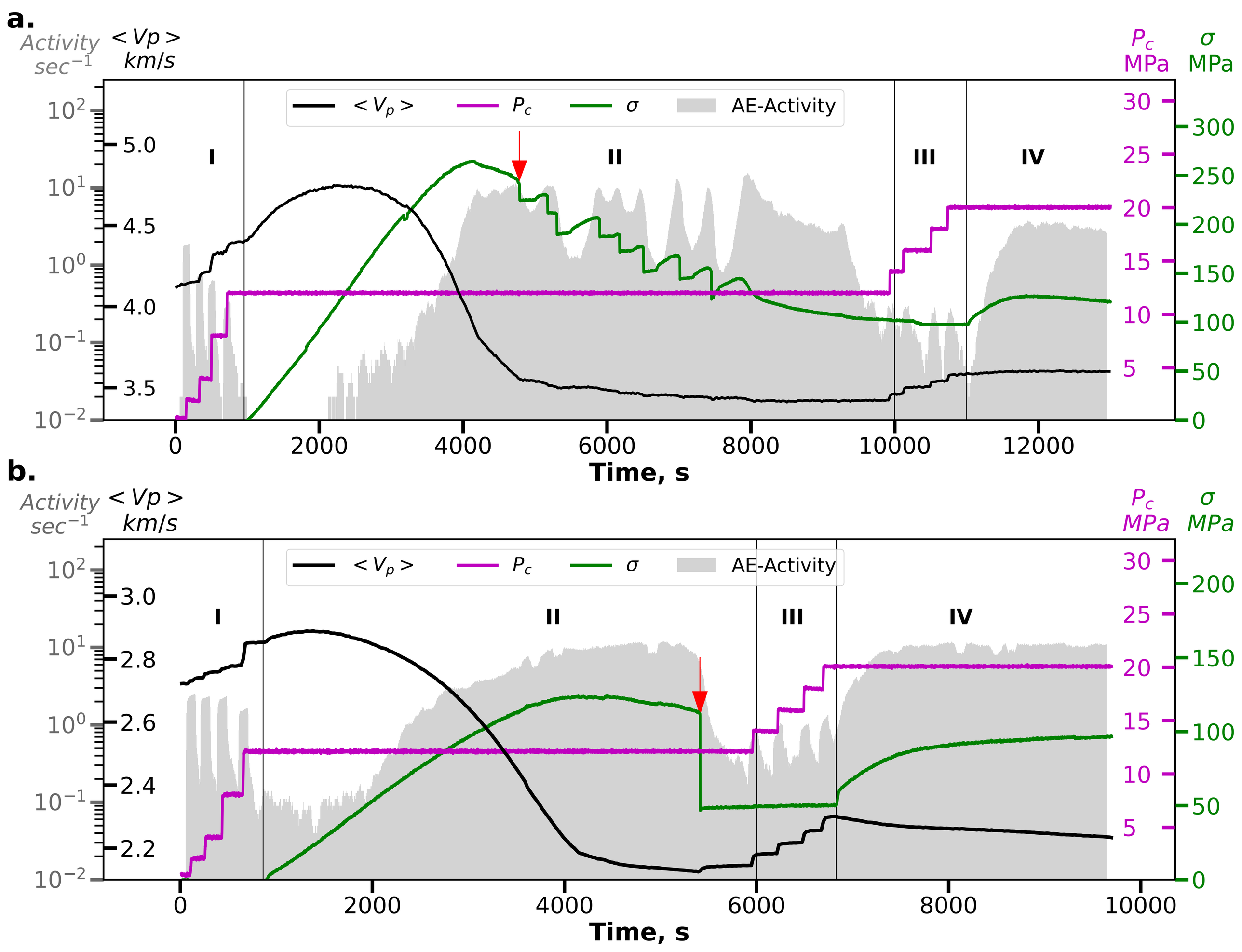
a.
Activity sec^{-1}
< Vp > km/s
P_c MPa
σ MPa
< V_p >
P_c
σ
AE-Activity
I
II
III
IV
Time, s
b.
Activity sec^{-1}
< Vp > km/s
P_c MPa
σ MPa
< V_p >
P_c
σ
AE-Activity
I
II
III
IV
Time, s

Figure3.

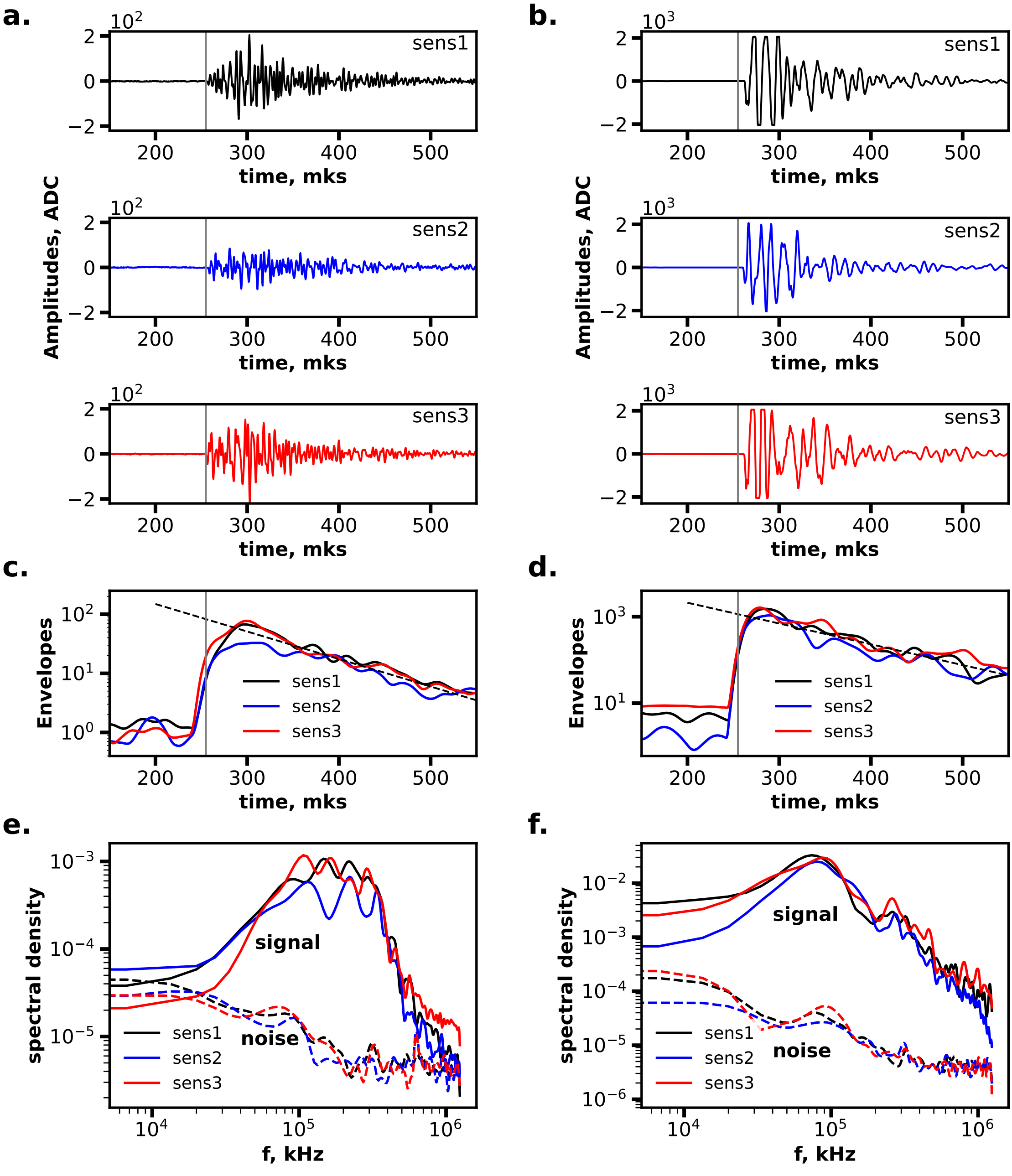
a.
b.
c.
d.
e.
f.
sens1
sens2
sens3
Amplitudes, ADC
time, mks
Envelopes
spectral density
f, kHz
signal
noise

Figure4.

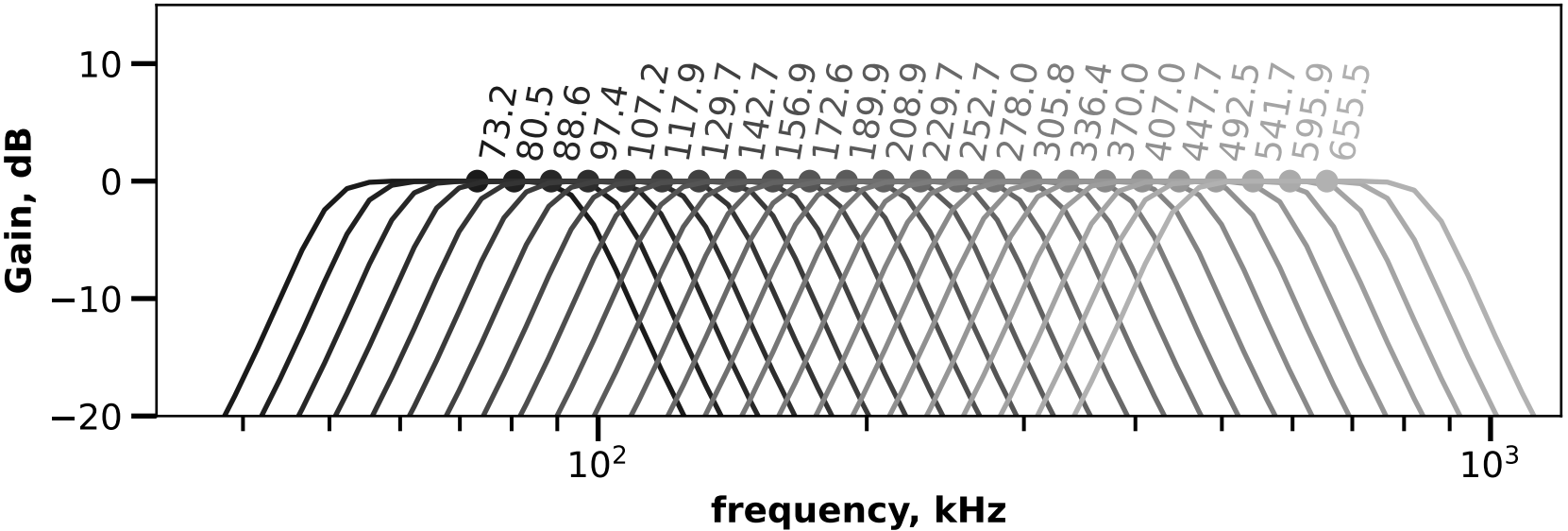
73.2
80.5
88.6
97.4
107.2
117.9
129.7
142.7
156.9
172.6
189.9
208.9
229.7
252.7
278.0
305.8
336.4
370.0
407.0
447.7
492.5
541.7
595.9
655.5
10
0
−10
−20
Gain, dB
10^2
10^3
frequency, kHz

Figure5.

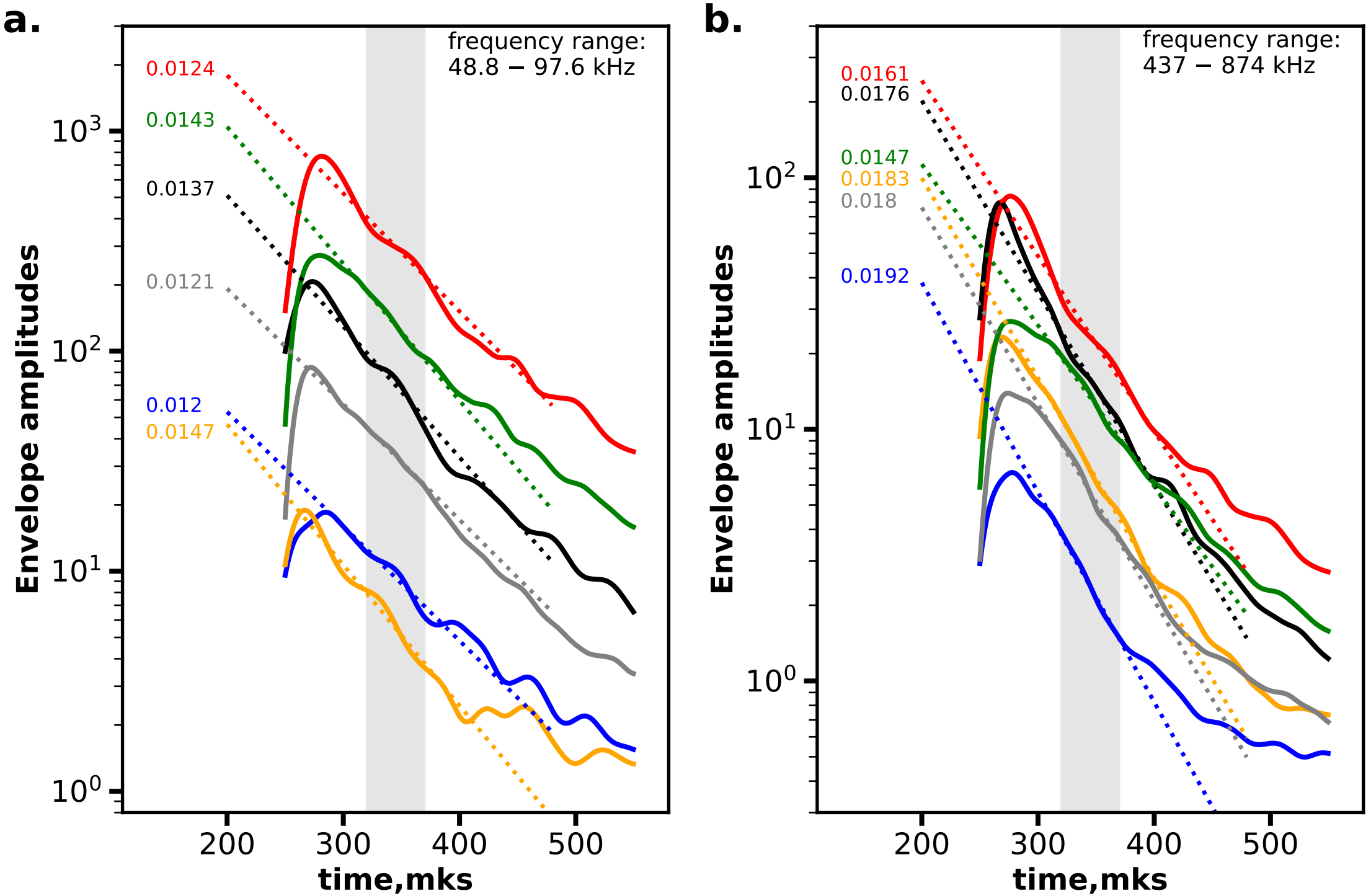
a.
frequency range:
48.8 − 97.6 kHz
0.0124
0.0143
0.0137
0.0121
0.012
0.0147
Envelope amplitudes
time,mks
b.
frequency range:
437 − 874 kHz
0.0161
0.0176
0.0147
0.0183
0.018
0.0192
Envelope amplitudes
time,mks

Figure6.

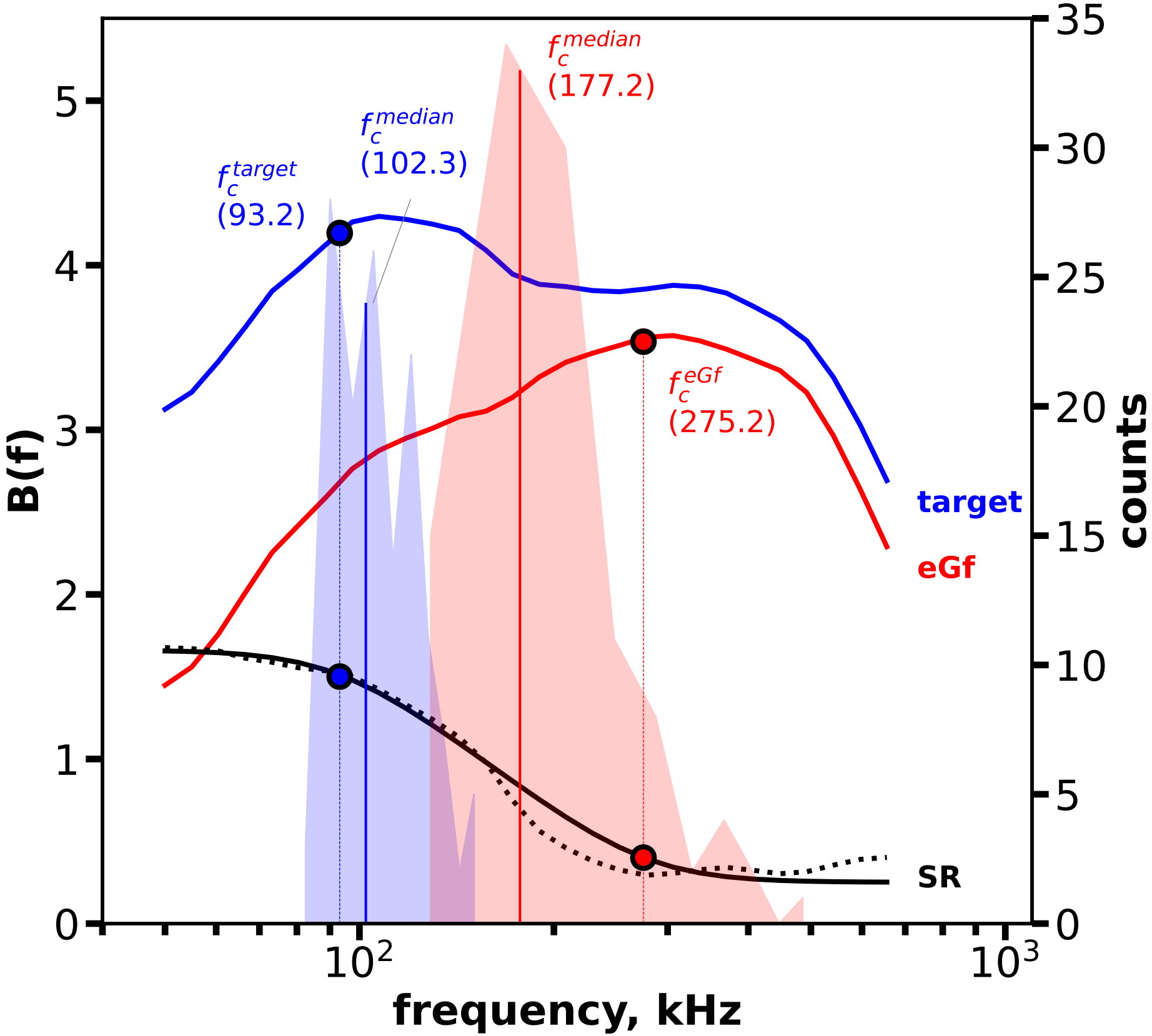
f_c^{median}
(177.2)
f_c^{median}
(102.3)
f_c^{target}
(93.2)
f_c^{eGf}
(275.2)
target
eGf
SR
B(f)
counts
frequency, kHz
0
1
2
3
4
5
0
5
10
15
20
25
30
35
10^2
10^3

Figure7.

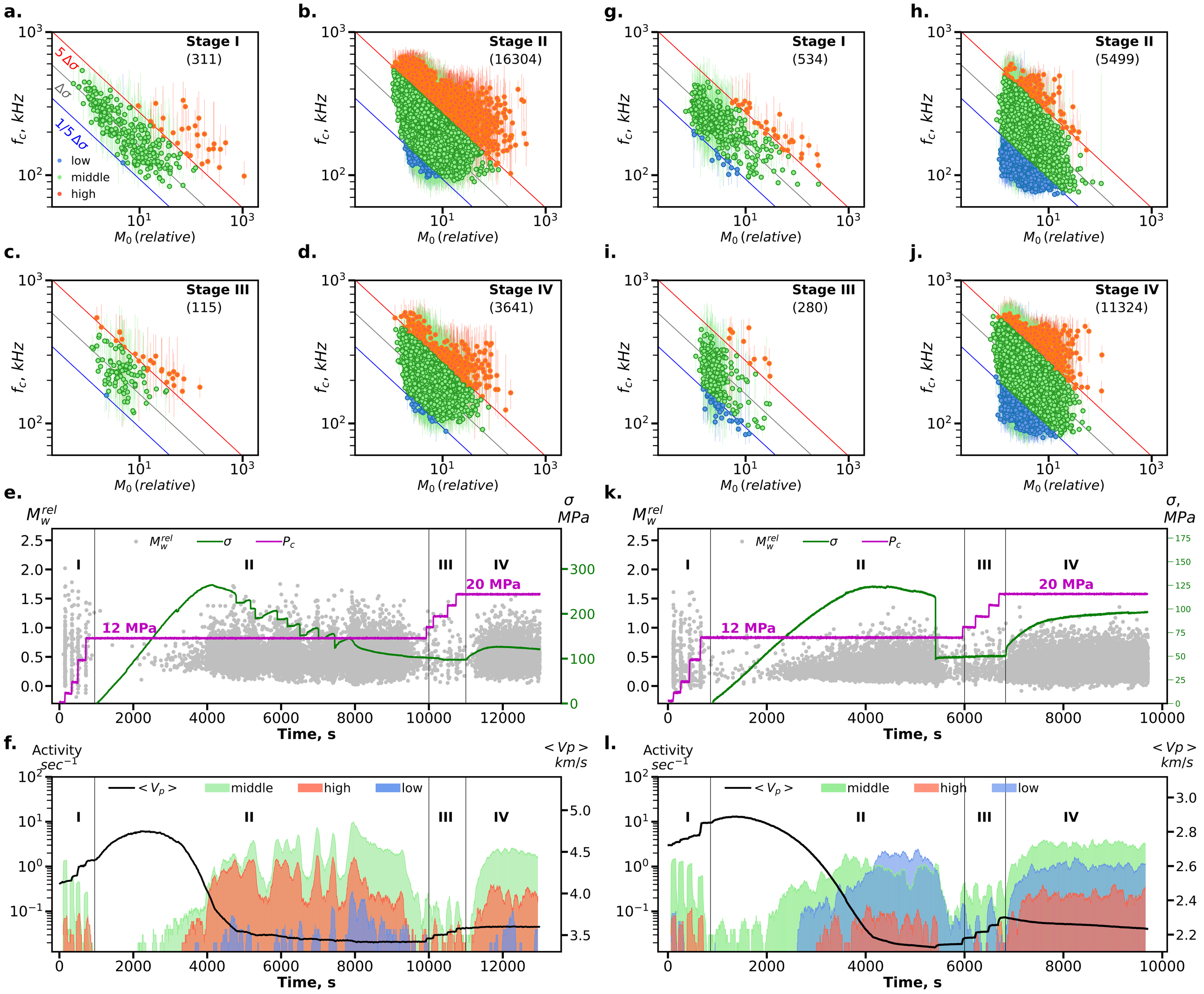
a.
Stage I
(311)
5 Δσ
Δσ
1/5 Δσ
low
middle
high
b.
Stage II
(16304)
g.
Stage I
(534)
h.
Stage II
(5499)
c.
Stage III
(115)
d.
Stage IV
(3641)
i.
Stage III
(280)
j.
Stage IV
(11324)
f_c, kHz
M_0 (relative)
e.
k.
M_w^{rel}
σ
MPa
P_c
12 MPa
20 MPa
I
II
III
IV
Time, s
f.
l.
Activity
sec^{-1}
< Vp >
km/s
$< V_p >$
middle
high
low

Figure8.

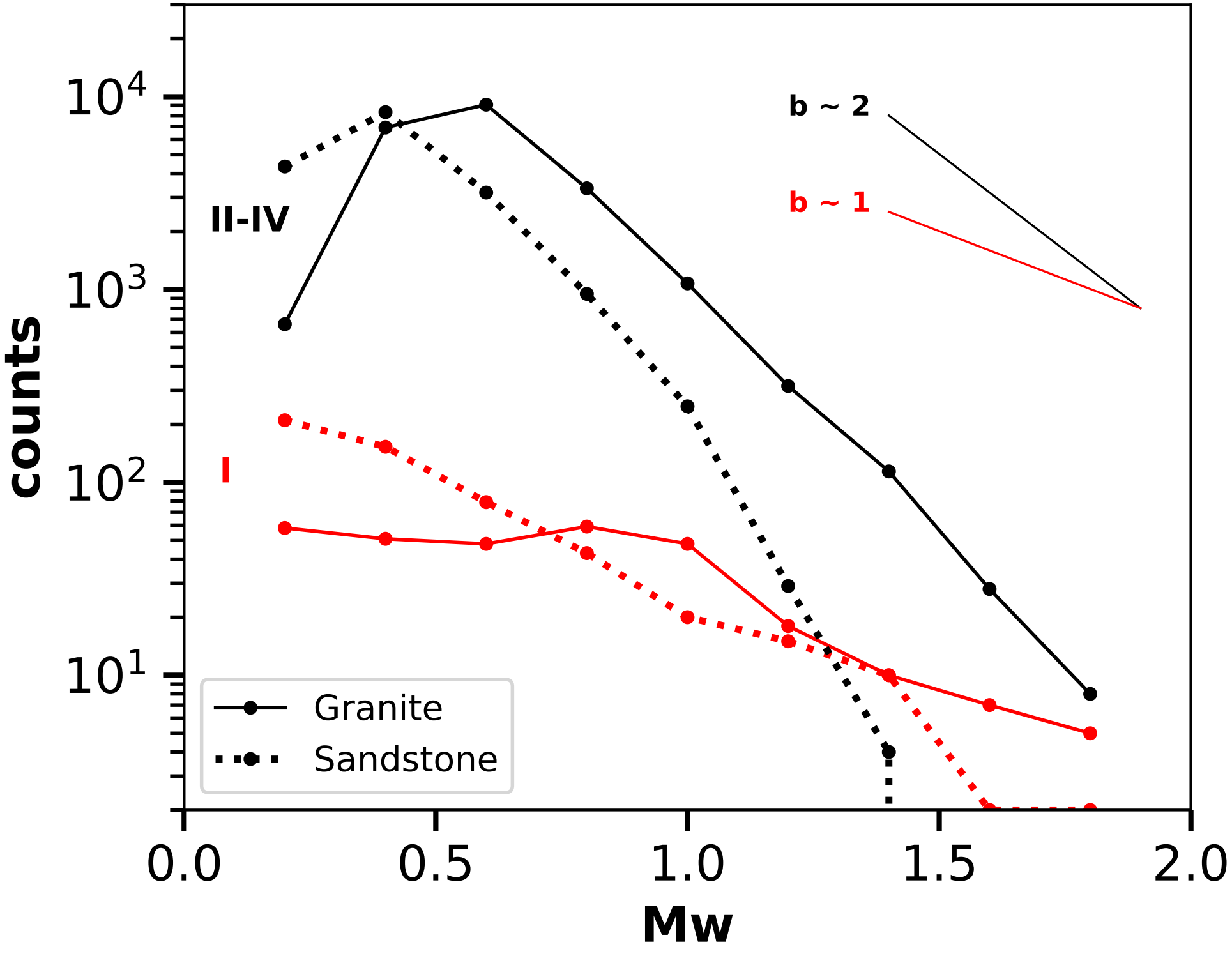
counts
Mw
10^4
10^3
10^2
10^1
0.0
0.5
1.0
1.5
2.0
b ~ 2
b ~ 1
II-IV
I
Granite
Sandstone

Figure9.

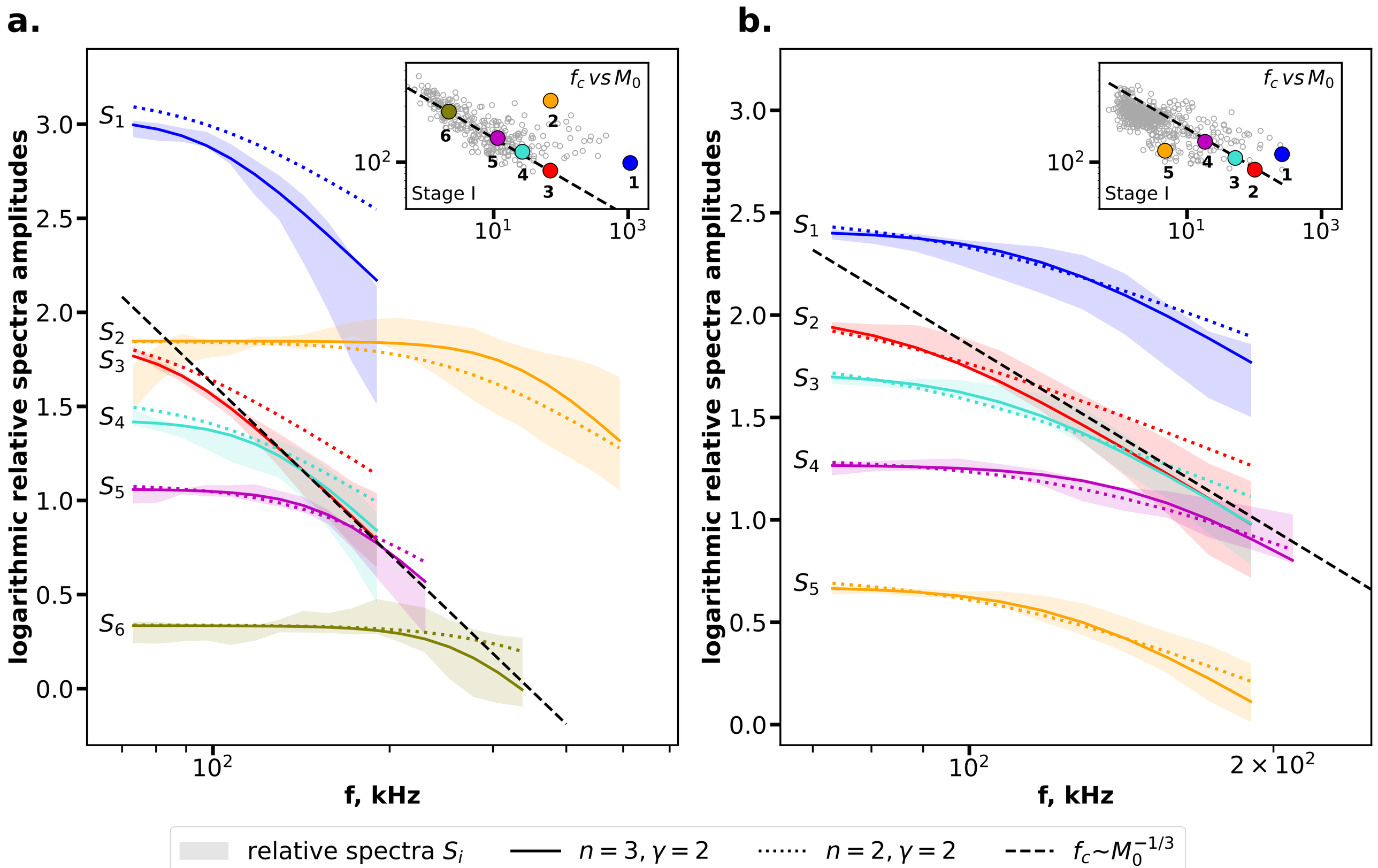
a.
b.
logarithmic relative spectra amplitudes
f, kHz
S_1
S_2
S_3
S_4
S_5
S_6
f_c vs M_0
Stage I
relative spectra S_i
$n = 3, \gamma = 2$
$n = 2, \gamma = 2$
$f_c \sim M_0^{-1/3}$

Figure10.

a.

Stage I

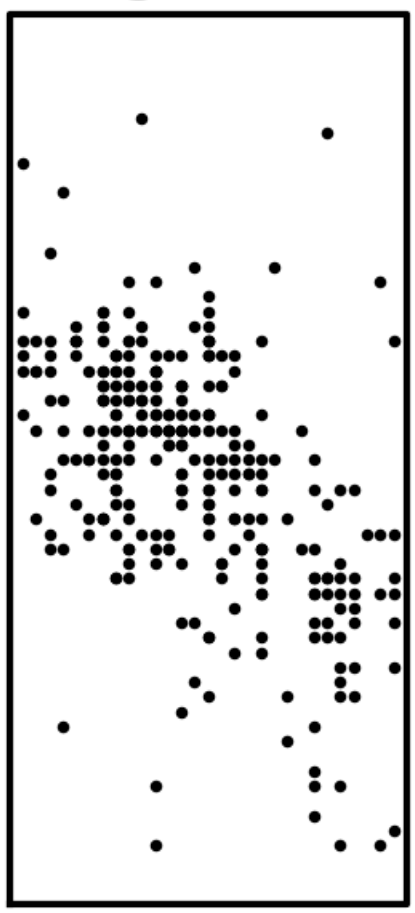

Stage II:
4700-5700s

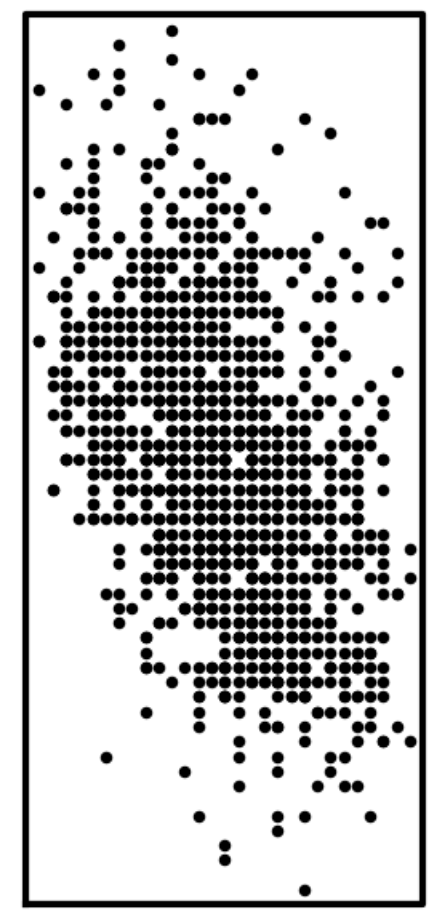

b.

Stage I

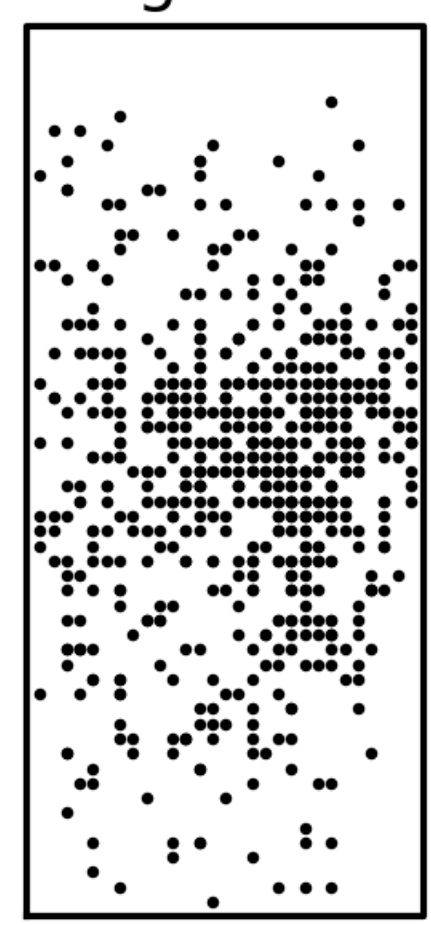

Stage II:
5400-6400s

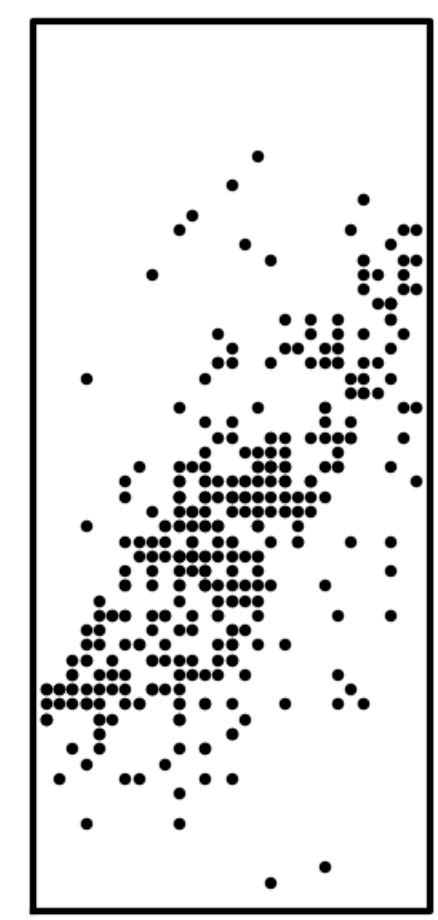

Figure11.

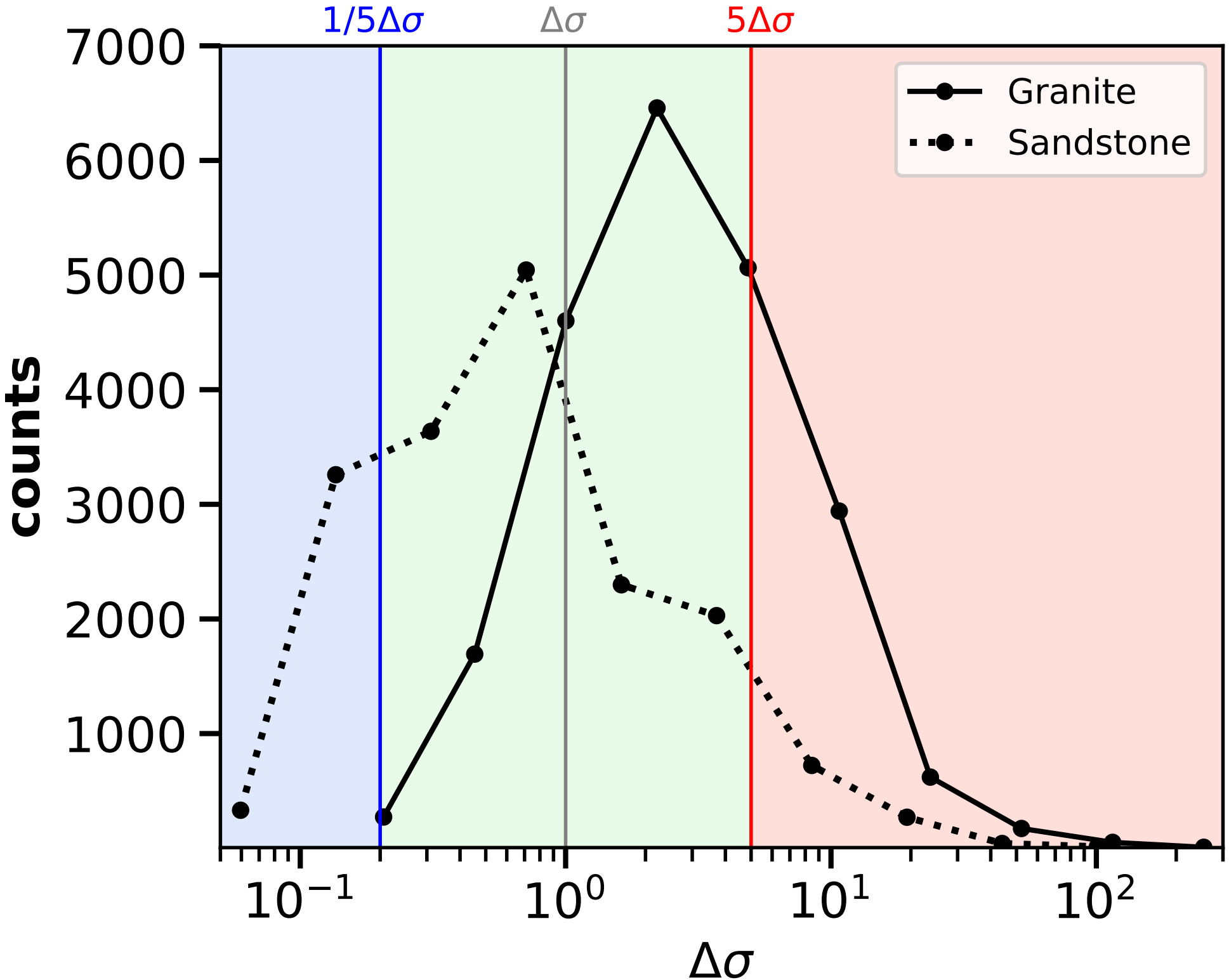
1/5Δσ
Δσ
5Δσ
Granite
Sandstone
counts
7000
6000
5000
4000
3000
2000
1000
10^{-1}
10^{0}
10^{1}
10^{2}
Δσ